International Journal of Plasticity 126 (2020) 102619

Contents lists available at ScienceDirect

International Journal of Plasticity

journal homepage: http://www.elsevier.com/locate/ijplas

Crystal plasticity modeling of the cyclic behavior of polycrystalline aggregates under non-symmetric uniaxial loading: Global and local analyses

Harris Farooq, Georges Cailletaud, Samuel Forest *, David Ryckelynck **

MINES ParisTech, PSL University, Centre des Matériaux, CNRS UMR 7633, BP 87, 91003, Evry, France

ARTICLE INFO

Keywords:
Multiscale modeling
Crystal plasticity
Finite element
CPFEM ratcheting
Mean stress relaxation
Strain distribution
Fatigue

ABSTRACT

When a sample is cyclically loaded under a mean stress or strain, incremental strain ratcheting or mean stress relaxation phenomena are usually observed. Experiments show that for metallic materials there is generally no full mean stress relaxation as well as saturation of macroscopic strain ratcheting. In contrast, most macroscopic constitutive models produce both quantities in excess, and complex sets of additional internal variables must be introduced to improve the modeling. Little attention has been paid to model such phenomena using polycrystal aggregates especially going up to the regime of cyclic mechanical stability. In this work based on an elementary crystal plasticity model for FCC crystals and large scale finite element simulations, it is shown that the interaction between different grains is sufficient to cater for such complex phenomena. Light is shed on how different regions of the polycrystal accommodate each other and how the classical definition of constant rate strain ratcheting or a zero mean stress is nearly impossible to apply to a polycrystalline aggregate. In addition, it is shown that even if a macroscopic stable hysteresis stress strain loop is observed, ratcheting phenomena can still be observed at the local scale. The distributions of different constitutive quantities within a polycrystal are also analyzed which gives a new insight into what is happening inside a polycrystal in terms of stress and strain redistribution. In particular, the existence of evolving bimodal distributions of stress and accumulated plastic strain is evidenced and related to the occurrence of plastic shakedown and incomplete mean stress relaxation. Two numerical criteria to detect strain ratcheting are finally proposed and discussed.

1. Introduction

Most metallic materials have a heterogeneous microstructure, and this local disorder results in specific mechanical properties. Several studies have been undertaken to link micro-macro properties of metals (Barbe et al., 2001; Dunne et al., 2007; Zhang et al., 2007, 2016; Guilhem et al., 2018), but how local properties affect macroscopic properties is still not fully understood. In particular, the behavior of metallic materials under cyclic loading conditions is the subject of considerable attention (Ghorbanpour et al., 2017; Smith et al., 2018; Yu et al., 2013). The present paper explores two topics, namely ratcheting and mean stress relaxation in polycrystalline

* Corresponding author.
** Corresponding author.
E-mail address: samuel.forest@mines-paristech.fr (S. Forest).

https://doi.org/10.1016/j.ijplas.2019.10.007
Received 11 July 2019; Received in revised form 24 October 2019; Accepted 25 October 2019
Available online 6 November 2019

aggregates under cyclic loading. Both phenomena result from asymmetric cyclic loading conditions. In this context, elastic shakedown refers to the material deforming plastically during the first few cycles and the subsequent response becomes elastic. Plastic shakedown refers to an open stabilized stress-strain hysteresis loop which does not move forward or backward on the strain axis. Asymmetric stress-controlled uniaxial cyclic loading can result in strain ratcheting, i.e. a progressive, incremental inelastic deformation leading to a shift of the stress-strain hysteresis loop along the strain axis (Fournier and Pineau, 1977; Jiang and Sehitoglu, 1994; Hassan and Kyriakides, 1994a,b; Ohno et al., 1998; Portier et al., 2000; Kang et al., 2010). Mean stress in this article is defined as $(\Sigma_{max} + \Sigma_{min})/2$ where Σ_{max} and Σ_{min} are the maximum and minimum applied stresses in a cyclically loaded component. The stress amplitude is defined as $(\Sigma_{max} - \Sigma_{min})/2$. With regards to asymmetric strain controlled cyclic loadings, it is also known that under a given stress amplitude, increasing the mean stress, or increasing the applied mean stress under constant amplitude, both increase the rate of ratcheting (Goodman, 1984). On the other hand, experimental observations indicate levels of mean stress for which there is very low ratcheting and the mechanical state of the material converges towards plastic shakedown (Pellissier-Tanon et al., 1982). Similarly, for asymmetric strain controlled loading conditions, a cyclic mean stress is observed, and several experimental studies (Wehner and Fatemi, 1991; Nikulin et al., 2019; Prithivirajan and Sangid, 2018) have deciphered the corresponding physical mechanisms. These observations show that for a given positive mean strain, and a low strain amplitude, the mean stress does not completely relax to zero. Also, increasing the strain amplitude leads to a nonlinear decrease of the mean stress until it finally vanishes (Arcari et al., 2009). From a modeling perspective, the mechanical cyclic response is sensitive to the strain path and is driven by the Bauschinger effect, as modeled by Chaboche (1986, 1989). Classical macroscopic models (Chaboche, 1989) predict an excess of strain ratcheting as well as mean stress. Some researchers have proposed to introduce additional kinematic and isotropic hardening terms (Chaboche et al., 2012), resulting in numerous material parameters to be calibrated. Any change in the material requires recalibration of parameters. Also, no microstructural characteristics of the underlying material are captured by such phenomenological models, which inhibits further inspection of the physics of deformation of the material. Crystal plasticity models coupled with computational homogenization, on the other hand, offer a way to link cyclic micro-macro properties of metallic materials (Shenoy et al., 2008). The deformation behavior of a single crystal at the slip system level is used to determine the properties of polycrystalline aggregates using representative volume elements. This procedure, although phenomenological at constitutive single crystal level, provides a realistic insight into what is happening within a polycrystal as shown by comparison between simulations and strain field measurements (Zhao et al., 2008b; Zaafarani et al., 2006).

Xie et al. (2004) and Sinha and Ghosh (2006), followed by Dingreville et al. (2010), were among the first authors to use polycrystalline aggregates coupled with CPFEM to model ratcheting. These researchers simulated the first few cycles and then extrapolated their results to larger cycle numbers. More recently, Hennessey et al. (2017) and Cruzado et al. (2017) proposed to change the kinematic hardening law from an Frederick and Armstrong (2007) formulation to a modified Ohno and Wang (1993) type law. Hennessey et al. use an accelerated simulation and run the simulation for a hundred cycles, while Cruzado et al. resort to a cycle jump technique (Cruzado et al., 2012; Azzouz et al., 2010; Mary and Fouvry, 2007) to extrapolate the constitutive response. Both groups focus on the macroscopic properties of the aggregate rather than on local stress and strain distributions. The main limitations of all the conducted studies are that local heterogeneity and the physics behind these phenomena are neglected in favor of focusing on the macroscopic stability of the stress-strain hysteresis loop. Attention is paid essentially to matching simulation and experimental results at the macroscopic level. In the recent contribution by Colas et al., 2019 the authors evidence local ratcheting phenomena in a polycrystalline aggregate under symmetric strain loading conditions. Local ratcheting phenomena are found to be more pronounced at a free surface than in the bulk. The analysis is however limited to one single realization, without statistical considerations.

The objective of the present work is to show that simulations of polycrystalline aggregates based on the most simple crystal plasticity laws can reproduce the main phenomenological features of asymmetric cyclic uniaxial plasticity and to correlate them with the stress and strain distributions inside the aggregates.

As stated earlier, the driving force for strain ratcheting and cyclic mean stress relaxation is the Bauschinger effect, which in a modeling perspective is governed by kinematic hardening. Kinematic hardening controls the ratcheting behavior as well as mean stress relaxation in structural components. Isotropic hardening, on the other hand, decreases the rate of plastic strain evolution per cycle. Single crystal behavior exhibits isotropic hardening effects due to multiplication and interaction of dislocations, as well as kinematic hardening as a result of polarization of dislocation structures. In a polycrystal, the cyclic response results from these two hardening components inside the grains and from the intergranular interactions. Hence, to assess these complex mechanisms, a very simple constitutive law is retained at the single crystal level for the systematic study of the present work. It is first limited to purely kinematic hardening. This is a simplification which complies with usual observations that isotropic hardening remains very limited in metallic alloys used for engineering purposes such as nickel-based superalloys under cyclic loading, which is the target material class of the present work (Chaboche et al., 2012). A rate–independent crystal plasticity model formulation is used to avoid the contamination of the final results by viscosity effects. The selected crystal plasticity model by (Forest and Rubin, 2016) exhibits a smooth elasto-plastic transition and is strictly rate-independent. In what follows, finite element simulations of polycrystalline aggregates will be shown to provide a realistic description of ratcheting and mean stress relaxation in face centered cubic (FCC) metals, without resorting to complex memory variables in contrast to macroscopic approaches. Two types of materials are taken into account, one with a low hardening limit and high yield strength similar to Nickel base superalloys, and a second one with stronger hardening and a low yield strength as seen in copper based alloys as a reference (Siska et al., 2007). Finally, the results are analyzed along two lines, i.e. at the macroscopic scale first and then at the local scale looking at field variables influencing the phenomena.

Three main original contributions discussed in this work must be pointed out: (1) the evidence that simulations of grain to grain interactions based on most simple single crystal model can predict limited ratcheting and mean stress relaxation phenomena, as observed in experiments; (2) the existence of bimodality in the stress-strain distribution functions inside the polycrystal and its

relations to the overall cyclic behavior; (3) the results are supported by large scale finite element simulations of polycrystalline aggregates up to large cycle number, namely 100 for the statistical analysis, more than 1000 for validation.

The paper is organized in the following manner. In Section 2 the crystal plasticity material model is formulated. Section 3 presents the finite element model, material parameters, as well as the physical aspects of the microstructure. Results and discussions are provided in Sections 4, regarding macroscopic aspects, and 5, regarding local stress and strain fields. They are followed by the conclusions in Section 6.

2. Crystal plasticity model

In the present work a small strain crystal plasticity formulation is used for the computation as most local strains remain below 5%. Each grain is considered as an initially homogeneous single crystal. To ease the interpretation of the numerical results, a rate–independent formulation is selected, using the single crystal plasticity model recently proposed by Forest and Rubin (2016). An advantage of using a rate–independent model coupled with a small strain assumption is the numerical efficiency which is crucial when simulating hundreds of cycles under various load amplitudes. In addition, it has been decided to use exclusively kinematic hardening because it governs ratcheting and mean stress relaxation. Face centered cubic (fcc) single crystal metallic materials comprising n plastic slip systems, each having a slip system direction $\boldsymbol{\ell}^s$ and a normal to the slip plane $\boldsymbol{n}^s$ are considered. The partition of the strain tensor introduces elastic and plastic parts:

$$\boldsymbol{\varepsilon} = \boldsymbol{\varepsilon}^e + \boldsymbol{\varepsilon}^p \tag{1}$$

The Hooke law relates the stress tensor to the elastic strain tensor. For cubic elasticity, a fourth rank tensor of elastic moduli $\boldsymbol{C}$, involving three independent parameters, governs the elastic behavior:

$$\boldsymbol{\sigma} = \boldsymbol{C}\boldsymbol{\varepsilon}^e \tag{2}$$

The plastic strain rate results from the slip processes with respect to all active slip systems,

$$\dot{\boldsymbol{\varepsilon}}^p = \sum_{s=1}^{n} \dot{\gamma}^s \boldsymbol{m}^s \tag{3}$$

with $\boldsymbol{m}^s$ being the Schmid orientation tensor defined as

$$\boldsymbol{m}^s = \frac{1}{2}(\boldsymbol{\ell}^s \otimes \boldsymbol{n}^s + \boldsymbol{n}^s \otimes \boldsymbol{\ell}^s) \tag{4}$$

The amount of slip on each slip system is denoted by the variable γ^s. The driving force for plastic slip on slip system s is the resolved shear stress, computed using the Cauchy stress tensor $\boldsymbol{\sigma}$ according to:

$$\tau^s = \boldsymbol{\sigma} : \boldsymbol{m}^s = \sigma_{ij} m_{ij}^s \tag{5}$$

The yield criterion is a generalization of Schmid's law involving scalar hardening variables r^s and x^s according to Méric et al. (1991).

$$f^s(\boldsymbol{\sigma}, x^s, r^s) = |\tau^s - x^s| - r^s \tag{6}$$

Here, r^s denotes the radius of the elastic domain and x^s is a scalar back-stress characterizing the center of the elastic range in the one-dimensional space of resolved shear stresses. In slip based crystal plasticity, there are n such elastic ranges. Plastic slip can occur only if the function f^s becomes positive. The viscoplastic flow rule given by Méric and Cailletaud (1991), is proposed in terms of the viscosity parameters, K and n:

$$\dot{\gamma}^s = \langle \frac{f^s}{K} \rangle^n \mathrm{sign}(\tau^s - x^s) \tag{7}$$

with the Macaulay brackets $< x > = \mathrm{Max}\,(x, 0)$. In the present work following Forest and Rubin (2016), the rate of slip on each slip system is replaced by a rate-independent formulation of the form:

$$\dot{\gamma}^s = \dot{\varepsilon} \langle \frac{f^s}{K} \rangle \mathrm{sign}(\tau^s - x^s) \tag{8}$$

where K is a positive constant having now the unit of stress and $\dot{\boldsymbol{\varepsilon}}$ is a non-negative homogeneous function of order one in the total strain rate. In this model, $\dot{\boldsymbol{\varepsilon}}$ is taken to be the total equivalent distortional strain rate:

$$\dot{\varepsilon} = \sqrt{\frac{2}{3}\dot{\boldsymbol{\varepsilon}}' : \dot{\boldsymbol{\varepsilon}}'}, \qquad \dot{\boldsymbol{\varepsilon}}' = \dot{\boldsymbol{\varepsilon}} - \frac{1}{3}(\mathrm{trace}(\dot{\boldsymbol{\varepsilon}}))\mathbf{1} \tag{9}$$

where $\boldsymbol{\varepsilon}'$ is the deviatoric part of the total strain rate tensor $\dot{\boldsymbol{\varepsilon}}$ and $\mathbf{1}$ the unit. Since the rate of inelasticity is linear in the total equivalent strain rate $\dot{\boldsymbol{\varepsilon}}$, all the evolution equations in the proposed theory are homogeneous of order one in time, characterizing a rate-independent response. Also, the rate of inelasticity is used for all states entailing no need for special treatment of loading and

Table 1
The 12 octahedral FCC slip systems numbered in the same order as they are defined in the code.

Slip system	Slip plane normal	Slip direction
1	(111)	$[\bar{1}01]$
2	(111)	$[0\bar{1}1]$
3	(111)	$[\bar{1}10]$
4	$(1\bar{1}1)$	$[\bar{1}01]$
5	$(1\bar{1}1)$	[011]
6	$(1\bar{1}1)$	[110]
7	$(\bar{1}11)$	$[0\bar{1}1]$
8	$(\bar{1}11)$	[110]
9	$(\bar{1}11)$	[101]
10	$(11\bar{1})$	$[\bar{1}10]$
11	$(11\bar{1})$	[101]
12	$(11\bar{1})$	[011]

unloading conditions. In particular no consistency condition is needed in contrast to standard rate–independent plasticity. The amplitude of the overstress is controlled by the value of parameter K. It tends to zero for vanishing values of K. There is no indeterminacy in the selection of active slip systems according to the present model. The functional form of f and the evolution equations for isotropic (r^s) as well as kinematic (x^s) hardening remain unchanged compared to the original model (Méric and Cailletaud, 1991). The accumulated slip variable v^s is defined for each slip system by the following evolution equation:

$$\dot{v}^s = |\dot{\gamma}^s| \tag{10}$$

The evolution equations for the kinematic hardening variable is taken from Méric et al. (1991) and Busso and Cailletaud (2005) without modification. The nonlinear kinematic hardening evolution law

$$\dot{x}^s = C\dot{\gamma}^s - D\dot{v}^s x^s \tag{11}$$

depends on two material parameters, C and D. In the present paper, there is no isotropic hardening so that the variable r^s has a constant value R_0, which corresponds to the initial resolved shear stress. Under monotonic loading Eq. (11) can be integrated into an exponential function with maximal value $x = C/D$ (Besson et al., 2009), called saturated value. As a result, the satured value of the critical resolved shear stress is $R_0 + C/D$.

Two crystal plasticity parameter sets were chosen, as stated in Table 2, where the saturated resolved shear stress is the same (i.e. $R_0 + C/D = 420$ MPa for both parameter sets); The difference however lies in the flipping of kinematic hardening and initial critical resolved shear stress. Parameter set 'LK' has a low kinematic hardening but a high initial critical resolved shear stress resembling aerospace alloys such as Inconel where the saturated value of the kinematic hardening variable is around one third of the initial yield stress. Parameter set 'HK' resembles an alloy with a low yield stress and a strong hardening such as copper where the saturated value of the kinematic hardening variable is three times that of the initial yield stress (Siska et al., 2007). Both parameter sets pertain to unit cells made of FCC crystals deforming plastically on octahedral slip systems {111}⟨110⟩. The slip systems, as ordered in the implicit simulation software Z–set package (2013), are given in Table 1.

3. FE model description

Literature findings show that the macroscopic representation of a micro-heterogeneous metallic material can be achieved with as few as one hundred grains (Barbe et al., 2001; Kanit et al., 2003; Bouchedjra et al., 2018), but matching macroscopic properties is not the goal. The goal here is to have a large enough statistical database so that local material response can be analyzed. The question of

Table 2
Crystal plasticity parameters used for both parameter sets. The saturated critical resolved shear stress is the same for both parameter sets; The only difference being that parameter set LK has a low kinematic hardening and high critical resolved shear stress and vice versa.

-	Parameter set LK	Parameter set HK
Cubic elasticity	$C_{1111} = 259600$ MPa	$C_{1111} = 259600$ MPa
	$C_{1122} = 179000$ MPa	$C_{1122} = 179000$ MPa
	$C_{1212} = 109600$ MPa	$C_{1212} = 109600$ MPa
Critical resolved shear stress	$R_0 = 320$ MPa	$R_0 = 100$ MPa
Kinematic hardening	C = 100000 MPa	C = 320000 MPa
	D = 1000	D = 1000
Overstress	K = 9 MPa	K = 9 MPa

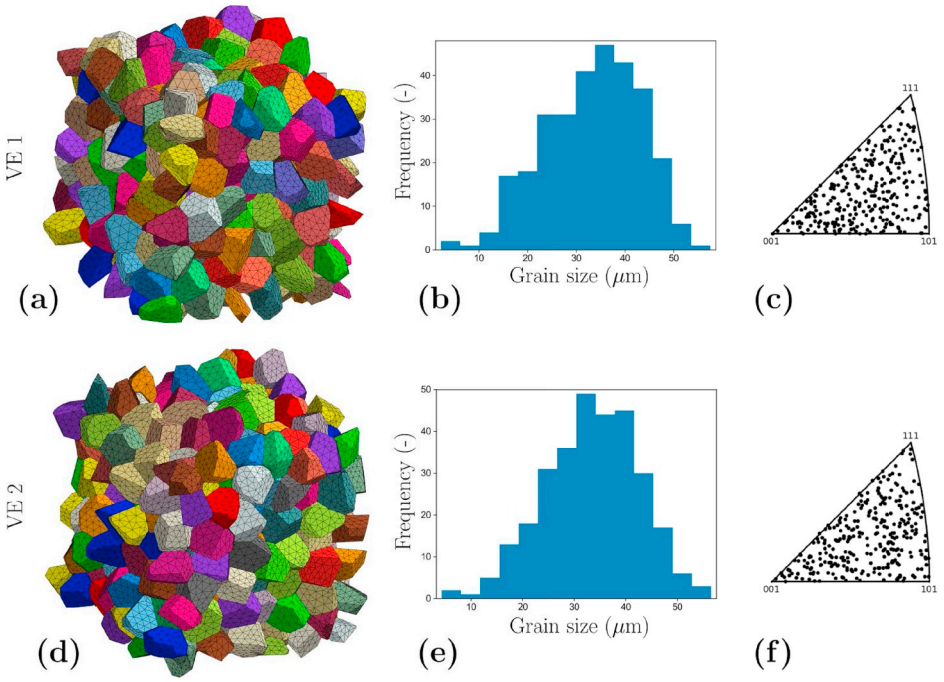

Fig. 1. 300 grain polycrystals for the FE simulations, along with the inverse pole figures of the crystallographic orientations used in the VEs.

choice of number of grains to be considered in the polycrystal is important in mechanics of heterogeneous media. Following guidelines by Kanit et al. (2003), about the definition of a Representative Volume Element (RVE) for random composite materials, a statistical approach is used consisting in selecting several realizations of the microstructure with a finite number of grains. Such polycrystal geometries are called Volume Elements (VE). Due to extremely long simulation times under cyclic loading, only 2 such volumes are considered. This is sufficient for a first estimate of the scatter of our predictions. It will be checked that both VEs give very close mechanical responses both at the macroscopic (overall curves) and local scales (strain distribution functions). In that sense, our method can be called an RVE approach. Two aggregates containing equiaxed grains, respectively called VE1 and VE2, were generated using the Voronoi tessellation technique with the help of the software VORO++ (Rycroft, 2009). A periodicity constraint was applied to obtain periodic microstructures. The software Gmsh was used to mesh both geometries, enforcing conditions of periodicity for the obtained meshes. Both aggregates contain 300 grains and reduced quadratic tetrahedral elements C3D10. The mesh of VE1 contains 194903 nodes and 130171 elements whereas the mesh of VE2 is made of 192042 nodes and 128166 elements (see Fig. 1 (a) and (d)). Each tetrahedral finite element has 10 nodes and 4 Gauss points.

The grain sizes in both VEs (as seen in Fig. 1 (b) and (e)), have a normal distribution with the crystal orientations uniformly distributed in the polycrystal (Fig. 1 (c) and (f)).

3.1. Computational requirements

The implicit finite element solver (Z–set package, 2013) is used to solve the problem. The global equilibrium is solved using a Newton-Raphson algorithm. Integration of constitutive equations at the Gauss points is performed using the second order Runge-Kutta method with automatic time stepping (Besson et al., 2009). For a crystal plasticity simulation, loading one job of the present size requires 31.5 gigabytes RAM. The MPI parallel computing algorithm implemented in Zebulon is used with 4 processors for each job. Each job requires around 24 h to complete one cycle and to run one hundred cycles, it required 100 days each. More than 320 simulations are being post-processed for this paper, while the actual number of calculated test cases is at least fifty times more than this. Given the number of degrees of freedom of each mesh and the cyclic nature of the problem, data of more than 20 TBytes were generated.

3.2. Boundary conditions

In the article, $\boldsymbol{\varepsilon}$ will be used to refer to the local strain tensor, and $\boldsymbol{E}$ will point to the macroscopic symmetric second-rank strain tensor defined as the average strain over the whole volume:

$$< \boldsymbol{\varepsilon} >= \frac{1}{V}\int_V \boldsymbol{\varepsilon} dV = \boldsymbol{E} \tag{12}$$

Similarly, $\boldsymbol{\sigma}$ will be the local stress tensor and the macroscopic stress $\boldsymbol{\Sigma}$ will be defined as its spatial average as follows:

$$< \boldsymbol{\sigma} >= \frac{1}{V}\int_V \boldsymbol{\sigma} dV = \boldsymbol{\Sigma} \tag{13}$$

Periodic boundary conditions were prescribed on the VEs such that the displacement vector field $\boldsymbol{u}$ over the entire volume takes the form:

$$\boldsymbol{u} = \boldsymbol{E}\cdot\boldsymbol{x} + \boldsymbol{v} \qquad \forall \boldsymbol{x} \in V \tag{14}$$

where the fluctuation $\boldsymbol{v}$ is periodic. This fluctuation takes the same value for each pair of homologous points at ∂V. Anti-periodic boundary conditions are prescribed to the traction vector $\boldsymbol{\sigma}.\boldsymbol{n}$ where $\boldsymbol{n}$ is the outer normal to ∂V at $\boldsymbol{x}$. The displacement and traction vectors are assumed to be continuous at the grain boundaries. For strain ratcheting, the macroscopic stress component Σ_{11} was imposed, whereas for mean stress relaxation the macroscopic strain component E_{11} was controlled. In both cases, all remaining volume averaged stress components are fixed to zero i.e. $\Sigma_{22} = \Sigma_{33} = \Sigma_{12} = \Sigma_{23} = \Sigma_{31} = 0$.

4. Results at macroscopic scale

This section presents the results obtained at a global level by averaging the stress and strain fields on the whole aggregate. Two loading types are investigated leading to ratcheting and mean stress relaxation respectively. In each case, the response obtained with a single crystal is given as an elementary reference.

4.1. Ratcheting in single crystals

The simulations of this subsection are performed at the material point level assuming homogeneous deformation. A uniaxial cyclic stress was imposed on the material element. Depending on the stress amplitude ($\Delta\Sigma/2$) and the mean stress $\overline{\Sigma}$, the resulting cyclic behavior can be broken down into three distinct responses i.e. elasticity, elastic shakedown and ratcheting. These three regions depend on the single crystal hardening parameters i.e its yield stress, and the kinematic and isotropic hardening parts. For a single crystal, yield stress in tension refers to the critical resolved shear stress divided by the Schmid factor. Fig. 2 depicts these regimes in a stress amplitude ($\Delta\Sigma/2 = (\Sigma_{max} - \Sigma_{min})/2$) vs mean stress[1] ($\overline{\Sigma} = (\Sigma_{max} + \Sigma_{min})/2$) diagram. This figure is schematic in the sense that the actual values on the two axes will depend on the crystal orientation. However, in the simplified model considered in this work where isotropic harening is neglected, the general shape of the diagram will always be the same. From Fig. 2, it can be seen that elastic shakedown refers to the material deforming plastically during the first few cycles and the subsequent response being elastic. Ratcheting in a single crystal is the progressive accumulation of strain per cycle without stopping, as signified by the red region. So depending on the loading type, a single crystal is bound to either ratchet or elastically shakedown. A missing region, as opposed to experimental observations, is that of plastic shakedown, which refers to an open stress-strain hysteresis loop which does not move forward on the strain axis. These three regimes can be classified as follows:

- Elastic if $\Delta\Sigma/2$ is smaller than the yield stress
- Shakedown if $\Delta\Sigma/2$ is smaller than the combination of the yield stress and the saturated isotropic hardening
- Ratcheting if $\Delta\Sigma/2$ is greater than the combination of the yield stress and the saturated isotropic hardening

4.2. Ratcheting in polycrystals

A periodic macroscopic stress (Σ_{11}) was imposed on polycrystalline volume element periodic boundary conditions. Two stress strain curves pertaining to the two parameter sets are shown in Fig. 3. The boundary conditions for both simulations are kept the same where $\Sigma_{max} = 1020$ MPa and $R_\Sigma = -0.7$. $R_\Sigma = \Sigma_{min}/\Sigma_{max}$ is the stress controlled loading ratio. To avoid clutter only the first ten cycles are plotted for both simulations. From the plot it can be seen that the curve for parameter set HK ratchets much more than the curve for parameter set LK because of the presence of a much higher kinematic hardening in the former.

Both simulations ratchet at different rates and comparing the accumulated axial strain can give a misleading estimation of what is ratcheting and what is shakedown. The same argument is valid for tests done at different amplitudes or loading ratios. Also, for a polycrystal, no matter how high the applied loading, the increment in accumulated strain $\Delta E = E_{n+1} - E_n$ always tends to decrease. This calls for the formulation of a robust test for discriminating ratcheting from shakedown. A test is proposed such that the delta accumulated strain per cycle is plotted (ΔE_{11}) against the number of cycles and identified with a power law series in the form:

$$E_{11}(N) = A\sum_{n=1}^{N}\frac{1}{n^\alpha} \tag{15}$$

where α is the slope of the series. The condition α larger than 1 is required for the power law series to converge. It follows that

[1] This definition is classical in fatigue but should not be confused with the same name given to the ratio between hydrostatic stress/divided by von Mises stress used in modeling ductile fracture.

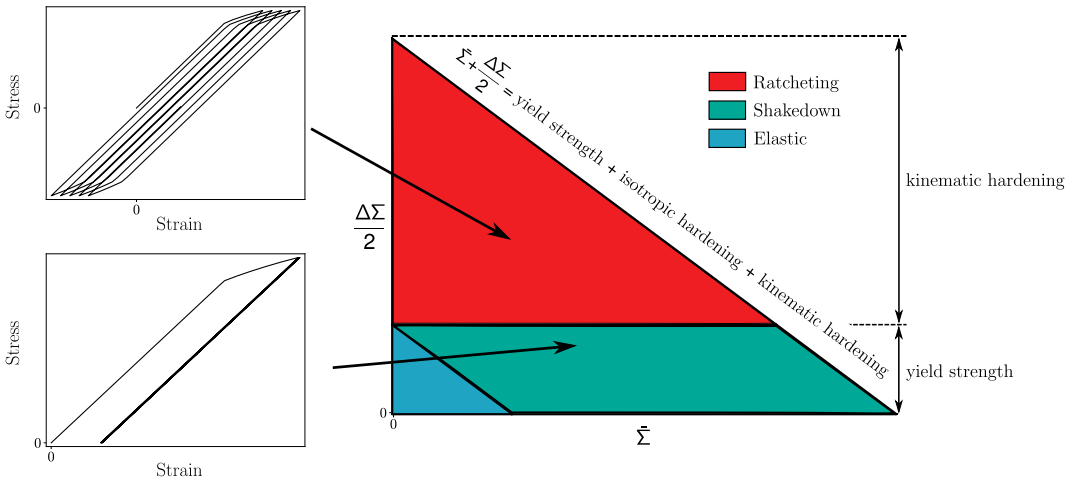

Fig. 2. Under asymmetric load control, the single crystal response which shows three distinct regions i.e. elastic, shakedown and ratcheting.

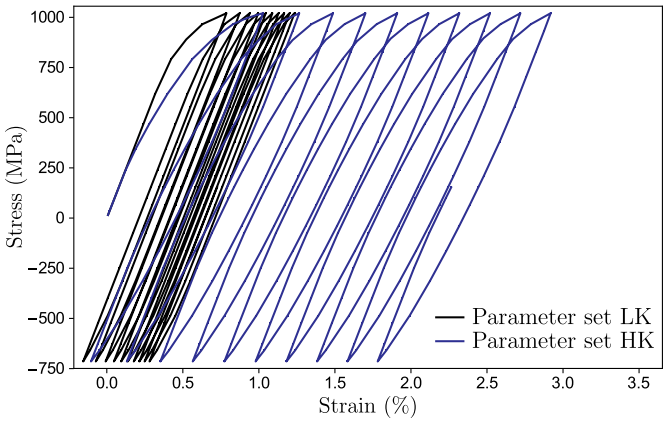

Fig. 3. For an asymmetric load controlled test, stress (Σ_{11}) vs strain (E_{11}) curves for both parameter sets. The loading conditions are kept the same for both i.e. $\Sigma_{max} = 1020$ MPa and $R_\Sigma = -0.7$. Only the first ten cycles are plotted in each case.

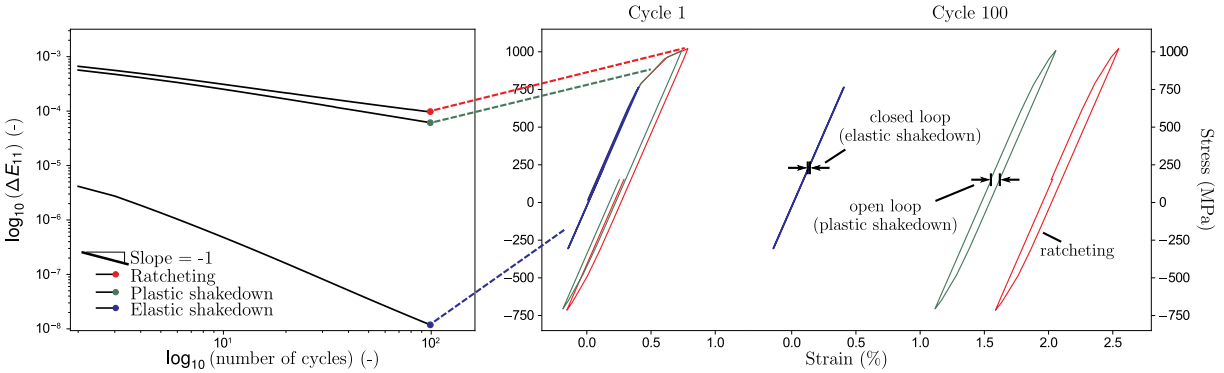

Fig. 4. For asymmetric load controlled tests, the left figure shows the evolution of the ratcheting strain increment as a function of cycle number for 3 polycrystal simulations using parameter set LK, with three different stress amplitudes. The macroscopic stress (Σ_{11}) vs strain (E_{11}) plot is shown on the right for three simulations showing the cyclic response at cycles 1 and 100. The simulations selected illustrate the elastic shakedown, plastic shakedown and ratcheting phenomena.

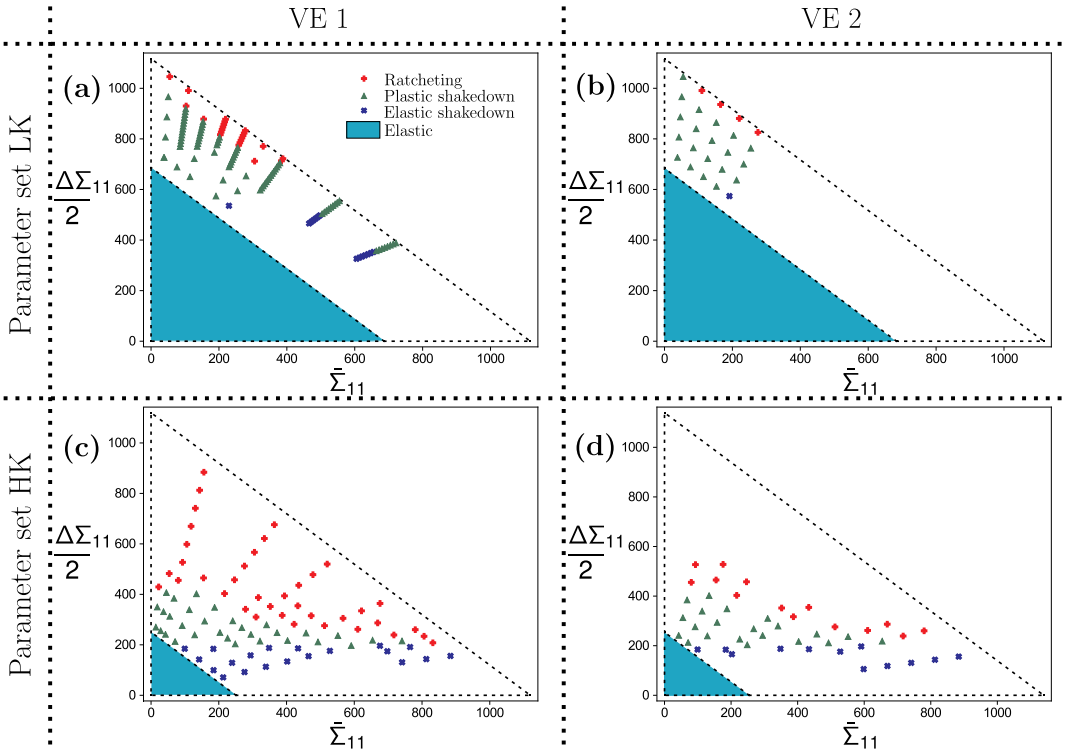

Fig. 5. Ratcheting maps in polycrystals (a) VE 1 and parameter set LK, (b) VE 2 and parameter set LK, (c) VE 1 and parameter set HK, (d) VE 2 and parameter set HK. The blue, green and red dots respectively denote elastic shakedown, plastic shakedown and ratcheting. (For interpretation of the references to color in this figure legend, the reader is referred to the Web version of this article.)

$$\text{the test series} \begin{cases} \text{converges}, & \text{if } \alpha \geq 1. \\ \text{diverges}, & \text{if } \alpha < 1. \end{cases} \tag{16}$$

The left plot in Fig. 4 shows 3 simulations that were run for parameter set LK for three different stress amplitudes. For comparison, a slope of -1 is also plotted on the left corner. The series test was performed after running the simulations for a hundred cycles each. There is a clear difference between a curve that will converge (shakedown) or one that will diverge (ratchet). As a second criterion, the second derivative at cycle 100 is also computed for all curves which indicates the convexity (ratcheting) or concavity (shakedown) of the curves. After applying the convergence or divergence criteria, the converging test cases are broken into two parts depending on whether or not the width of the stress strain loop is open or closed at cycle 100. An open loop signifies that there is plastic shakedown, whereas a closed loop points to elastic shakedown. A small offset of tolerance is needed to establish what is meant by a closed loop. In the present work, the tolerance for the width of the loop at its mean stress is set to be $\delta = 1.0 \times 10^{-6}$. The right hand plot in Fig. 4 shows the macroscopic stress vs strain response for three selected cases at the first and at the hundredth cycle. It can already be established that the red curves are diverging while the green and blue curves are converging. Multiple simulations are run, on the polycrystal aggregates, at various load amplitudes and mean stresses for a hundred cycles each. Then the evolution of macroscopic strain in each

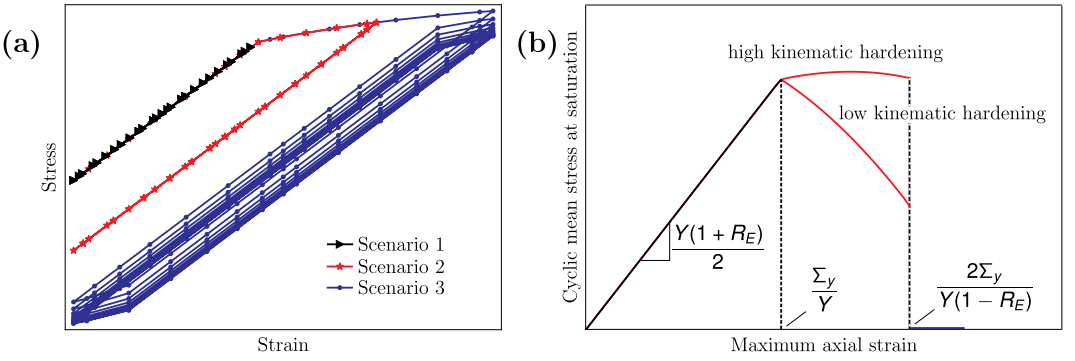

Fig. 6. For a single crystal under asymmetric strain controlled loading, (a) stress vs strain plot showing the three scenarios of cyclic mean stress relaxation, and (b) mean stress at saturation vs maximum axial strain plot.

simulation is assessed using the series comparison test, and a diagram similar to that of Fig. 2 is drawn for four cases i.e. for both VEs and for both parameter sets. Fig. 5 shows that this diagram differs from the single crystal case. Four regions can be seen i.e. elastic, elastic shakedown, plastic shakedown and ratcheting instead of three in the single crystal case. The elastic region is determined using the plasticity criterion for metals of a yield strength of 0.2% plastic strain E^p, and is characterized by the grey region. The maximum stress limit for the polycrystal is computed by applying a macroscopic strain of 4%, the resulting stress being taken to be the limit above which the material cannot be loaded i.e. the top and bottom right corner of each plot in Fig. 5. In the same figure, the dots are found to segregate into three regions, namely elastic shakedown, plastic shakedown and ratcheting respectively. For parameter set LK, the region in which ratcheting and plastic shakedown occur is very small because of the low kinematic hardening. Parameter set HK, on the other hand, leads to a much larger region for plastic shakedown and ratcheting. It should however be noted that the diagrams of Fig. 5 (a) and (b), as well as (c) and (d) are very similar signifying that it is both VEs can be regarded as representative microstructures capable of reproducing the typical cyclic mechanical behavior of the material.

4.3. Mean stress relaxation in single crystals

Under asymmetric cyclic strain control, the mean stress relaxes to a certain value when increasing the cycle number. At the macroscopic level, this mean stress $\overline{\Sigma}_{11}$, defined as $(\Sigma_{max} + \Sigma_{min})/2$, where Σ_{max} and Σ_{min} are the maximum and minimum stresses under peak strains. In this case, a single crystal cyclic response can be broken down into three distinct scenarios which are represented in Fig. 6 (a) and (b). Focusing on Fig. 6 (a), the first scenario shows the elastic regime where cyclic loading will have no effect on the cyclic mean stress redistribution. To remain in this regime plasticity has to be avoided i.e. the applied maximum strain (E_{max}) should be:

$$E_{max} < \frac{\Sigma_y}{Y}, \tag{17}$$

where Σ_y is the stress at which yielding starts and Y is the Young's modulus of the single crystal in the loading direction. Next, in the second scenario plasticity is observed only during the first tensile loading but upon unloading immediately after, elastic response is observed in the following cycles. To characterize the second scenario, the loading ratio R_E is defined as:

$$R_E = \frac{E_{min}}{E_{max}}, \tag{18}$$

where E_{min} is the minimum applied strain. Then, the maximum applied strain E_{max} in the second regime should be in the following interval:

$$\frac{\Sigma_y}{Y} < E_{max} < \frac{2\Sigma_y}{Y(1 - R_E)}, \tag{19}$$

in the absence of isotropic hardening. Finally in the last regime, the mean stress relaxes to zero and the maximum applied strain should be:

$$E_{max} > \frac{2\Sigma_y}{Y(1 - R_E)}. \tag{20}$$

Fig. 6 (b) then depicts the curve of the mean stress at saturation vs maximum applied axial strain. The first scenario corresponds to the initial straight line with a slope of $Y(1 - R_E)/2$; The second scenario depends on the type of kinematic hardening, and finally in the third scenario, a zero mean stress is found.

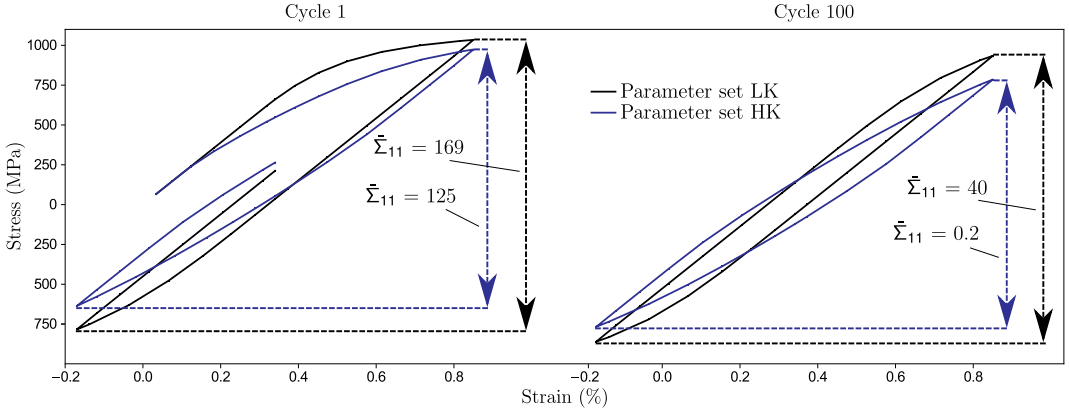

Fig. 7. Under asymmetric strain controlled boundary conditions on VE 1, stress (Σ_{11}) vs strain (E_{11}) plot for both parameter sets with $R_E = -0.2$, and $E_{11} = 0.85\%$. Responses were extracted at cycles 1 and 100 for both parameter sets. Cyclic mean stresses ($\overline{\Sigma}_{11}$) are also given for each case respectively.

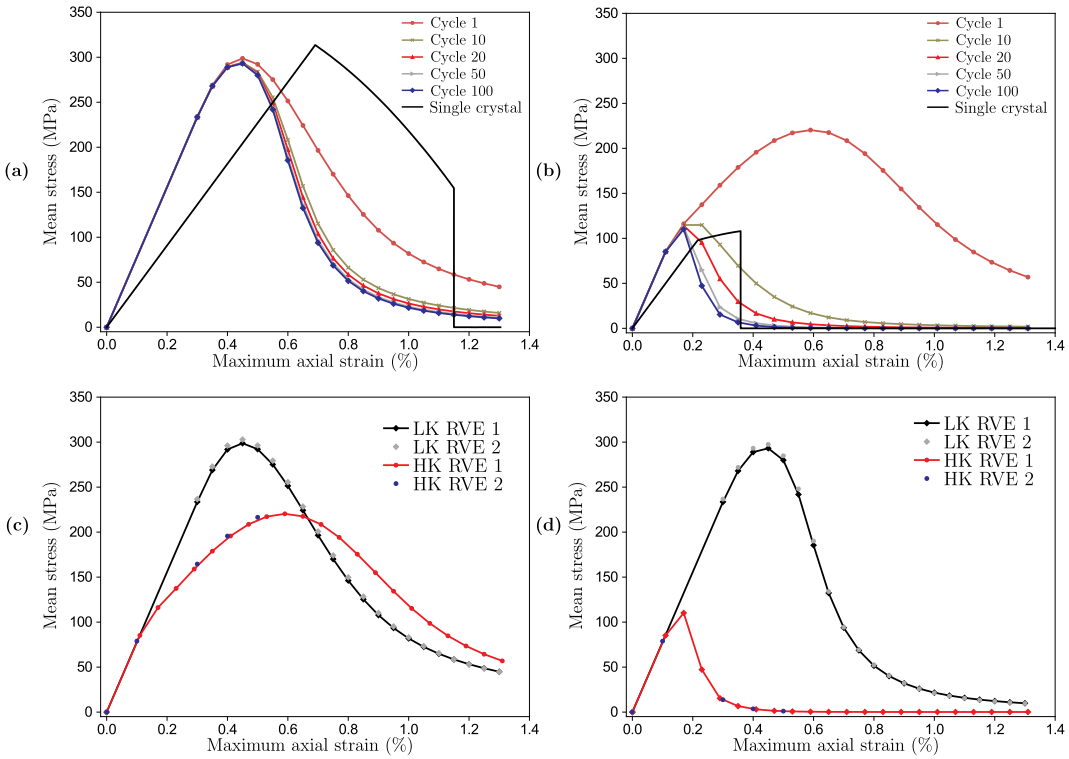

Fig. 8. Mean stress relaxation in polycrystals (a) VE 1, parameter set LK, (b) VE 1 parameter set HK, (c) comparison of VE 1 and 2 for parameter set LK and HK at cycle 1, (d) comparison of VE 1 and 2 for parameter set LK and HK at cycle 100. Comparison with single crystal response with lattice orientation <001 >, for figures (a) and (b).

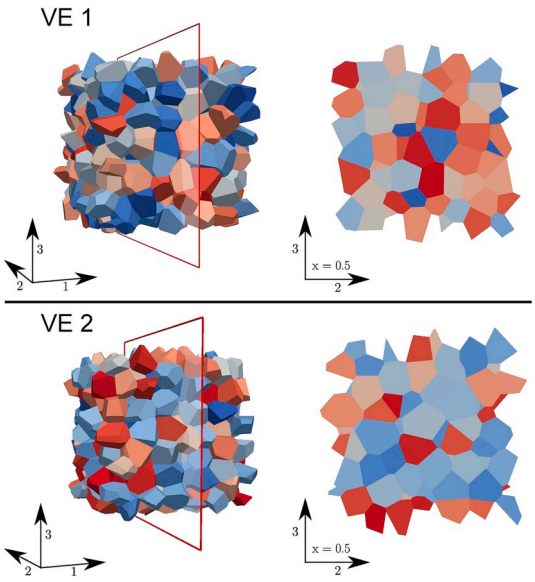

Fig. 9. A slice of VE 1 and 2 along the 2–3 plane, at x = 0.5.

4.4. Mean stress relaxation in polycrystals

The boundary conditions applied to the meshes of Fig. 1 were periodic with an average strain E_{11} imposed on all elements. Fig. 7 shows the average stress (Σ_{11}) vs strain (E_{11}) response for the two parameter sets on VE 1. Both VEs were submitted to the same loading conditions $E_{11} = 0.85\%$ and $R_E = -0.2$. It can be seen that at cycle 100, the curve for parameter set LK stabilizes to a mean stress of

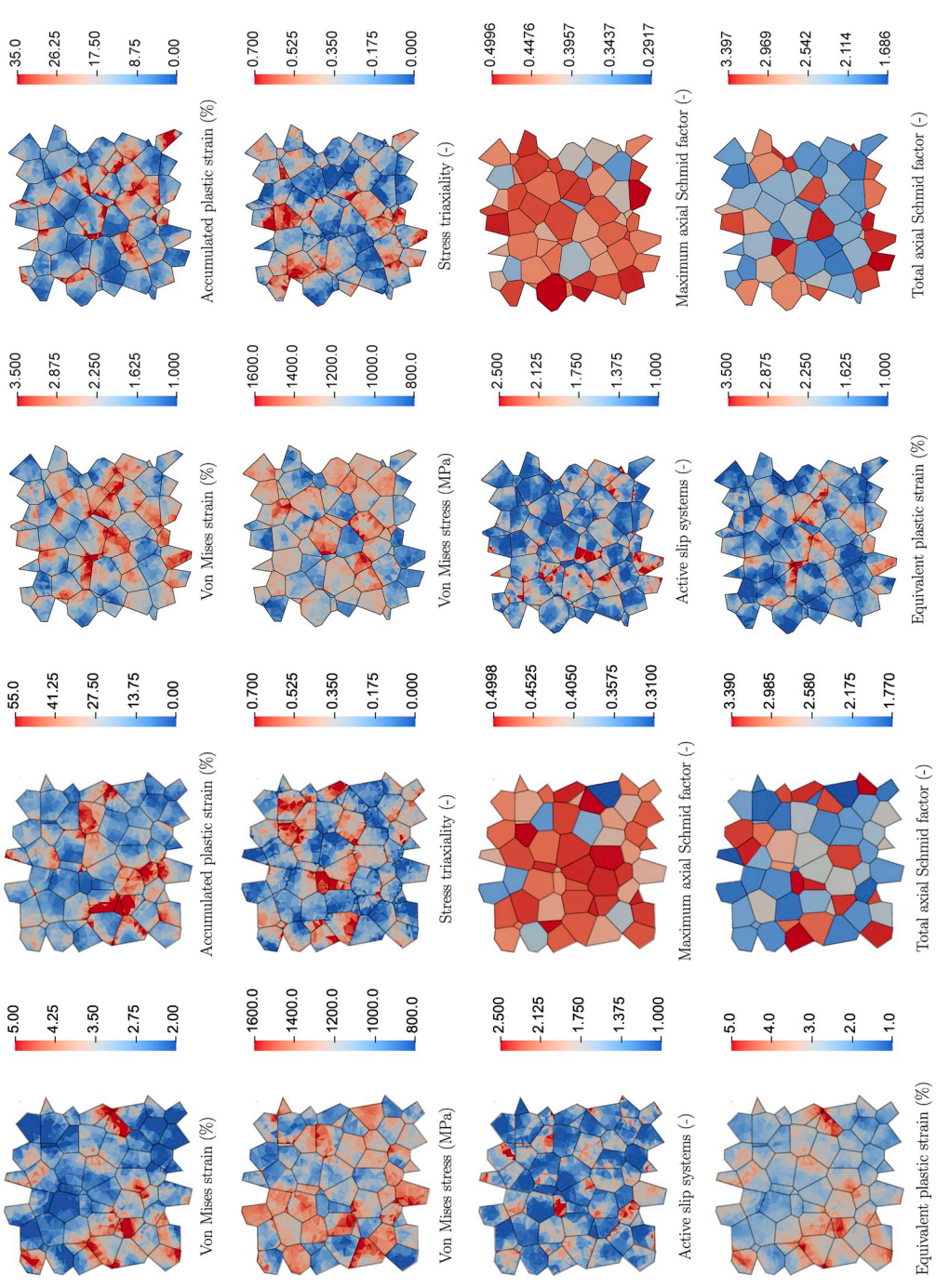

Fig. 10. a) For VE 1, contour plots of a simulation with $\Sigma_{11} = 1021$ MPa, and asymmetric load with $R_\Sigma = -0.7$ after running one hundred cycles, extracted at the maximum stress of the one hundredth cycle. The contour plots show the von Mises strain, accumulated plastic strain, equivalent plastic strain, von Mises stress, stress triaxiality, maximum slip divided by total slip, and the axial highest Schmid factor, and the total Schmid factor. Fig. 10: (b)For VE 2, contour plots of a simulation with $\Sigma_{11} = 1021$ MPa, and asymmetric load with $R_\Sigma = -0.7$ after running one hundred cycles, extracted at the maximum stress of the one hundredth cycle. The contour plots show the von Mises strain, accumulated plastic strain, equivalent plastic strain, von Mises stress, stress triaxiality, maximum slip divided by total slip, and the axial highest Schmid factor, and the total Schmid factor.

40 MPa, whereas the curve for parameter set HK relaxes to less than 0.5 MPa.

According to Fig. 8, the response of the polycrystal can be characterized by the mean stress vs maximum axial strain diagram. Each point represents one simulation, with 100 cycles each, and a total of 21 simulations were run ranging from $E_{11} = 0.3\%–1.3\%$ with R = − 0.2 for parameter set LK and VE 1. Similarly, 21 simulations ranging from $E_{11} = 0.11\%–1.31\%$ with R = − 0.2 were performed for parameter set HK and VE 1. Fig. 8 (a) and (b) show the response for parameter sets LK and HK. It can be seen how the cyclic mean stress relaxes with the number of cycles. The response of a single crystal oriented at ⟨001⟩ is also plotted for both parameter sets for comparison. In both cases, it was found that a steady state was achieved at cycle 100. Fig. 8 (c) and (d) shows the response of both VEs for each parameter set at cycle 1 and 100. It can be seen that parameter set LK does not lead to mean stress relaxation to zero even at a high maximum axial strain. In contrast the material with parameter set HK relaxes to zero for $E_{11} = 0.5\%$. It can be seen that, when compared to a single crystal, the polycrystal response displays a smooth transition between the three scenarios which conforms to experimental findings (Chaboche et al., 2012). In addition, both VEs produce a similar response suggesting that the considered volume elements are representative with respect to this macroscopic response.

5. Analysis of local results

Attention is now focused on intragranular response of the material. Two types of local results are considered here, namely contour plots of stress and plane strain fields, as well as Gauss point statistics. For the contour plots, VE 1 and 2 are sliced at x = 0.5, as depicted in Fig. 9.

5.1. Local ratcheting behavior

The results of one stress controlled simulation up to 100 cycles with $\Sigma_{11} = 1021$ MPa and $R_\Sigma = -0.7$ for both VE 1 and 2 are analyzed. They are plotted in Fig. 10 at the time step corresponding to the tensile peak of the one hundredth cycle. An overlay of the grain boundaries is also superimposed on top of each contour map to make the observations easier to interpret. Eight contour plots are shown for the following field variables:

- von Mises strain $\varepsilon_{vM} = \sqrt{\frac{2}{3}\boldsymbol{\varepsilon}'_{ij}\boldsymbol{\varepsilon}'_{ij}}$, where $\boldsymbol{\varepsilon}'$ is the deviatoric part of the local strain tensor,

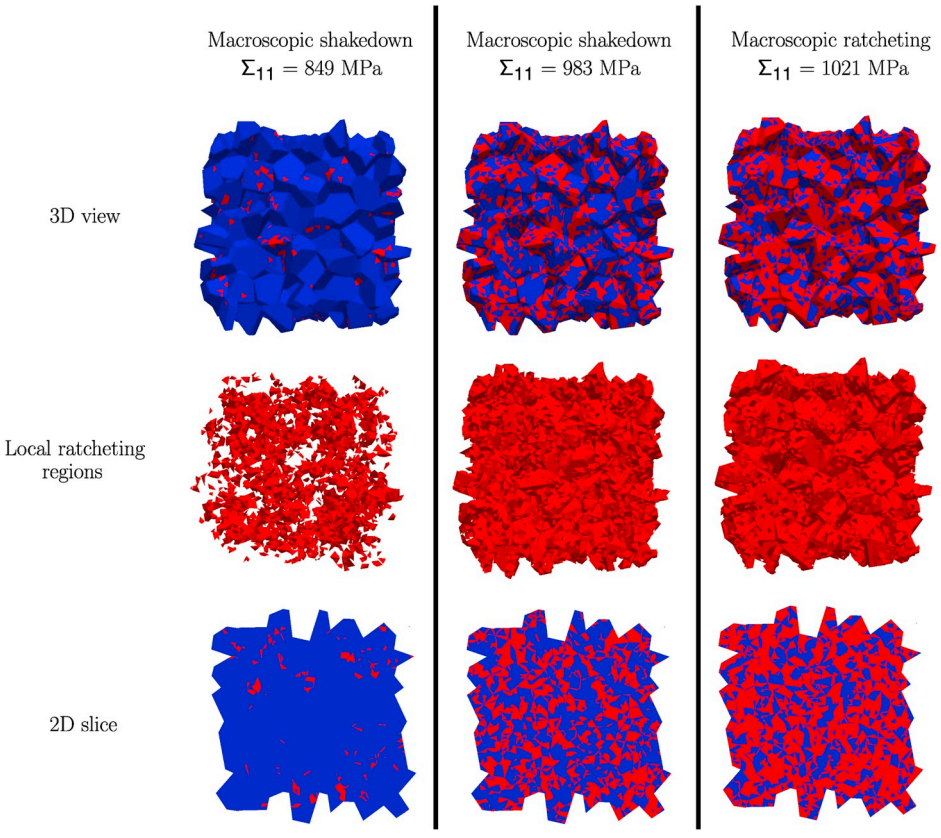

Fig. 11. Three different asymmetric stress controlled simulations with $\Sigma_{11} = 849$ MPa, $\Sigma_{11} = 983$ MPa, and $\Sigma_{11} = 1021$ MPa, and $R_\Sigma = -0.7$ for all cases (VE 1, parameter set LK). Macroscopically, the first and second shakedown while the third ratchets. Local regions for ratcheting and shakedown (per finite element) are respectively shown in red and blue for each case.

- equivalent plastic strain $\varepsilon^{p}_{eq} = \sqrt{\frac{2}{3}\boldsymbol{\varepsilon}^{p}_{ij}\boldsymbol{\varepsilon}^{p}_{ij}}$
- accumulated plastic strain $\varepsilon_{acc} = \int_0^t \sqrt{\frac{2}{3}\dot{\boldsymbol{\varepsilon}}_{ij}\dot{\boldsymbol{\varepsilon}}_{ij}}dt$,
- von Mises stress $\sigma_{vM} = \sqrt{\frac{3}{2}\boldsymbol{\sigma}^{'}_{ij}\boldsymbol{\sigma}^{'}_{ij}}$, where $\boldsymbol{\sigma}'$ is the deviatoric part of the local stress tensor,
- stress triaxiality $\sigma_{tri} = \frac{\boldsymbol{\sigma}_{ii}/3}{\sqrt{\frac{3}{2}\boldsymbol{\sigma}^{'}_{ij}\boldsymbol{\sigma}^{'}_{ij}}}$,
- number of active slip systems: $\left(\sum_{s=1}^{N}|\gamma^{s}|\right)\Big/\max_{s=1,N}(|\gamma^{s}|)$, where s is the slip system,
- maximum axial Schmid factor per grain $m_{\max} = \max_{s=1,N}(|m^{s}|)$, where $m^{s} = (\mathbf{n}^{s}.\mathbf{t})\,(\mathbf{l}^{s}.\mathbf{t})$, $\mathbf{t}$ being the tensile direction and s the slip system. This factor is computed assuming uniaxial tension.
- total axial Schmid factor per grain $m_{total} = \sum_{s=1}^{N}|m^{s}|$.

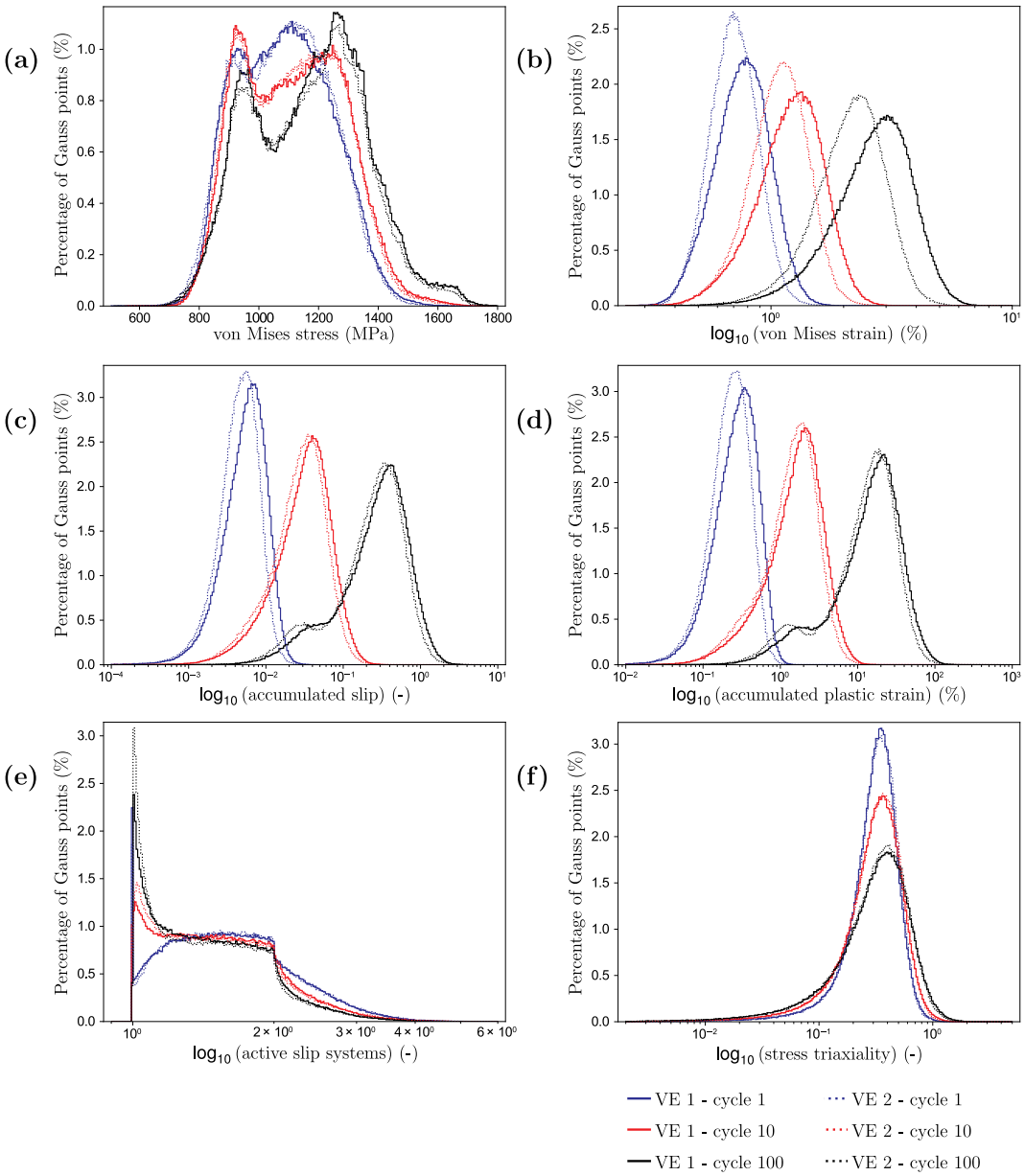

Fig. 12. Distribution curves of Gauss point variables for an asymmetric stress controlled test using parameter set LK, $R_{\Sigma} = -0.7$ and $\Sigma_{11} = 1021$ MPa. The variables shown are (a) von Mises stress (b) von Mises strain, (c) accumulated slip, (d) accumulated plastic strain, and (e) stress triaxiality.

For both VEs, the von Mises strain and equivalent plastic strain maps in Fig. 10 show that these quantities have very similar maps and it can be seen that they segregate in some regions of the microstructure. These regions do not specifically conform to any specific grain or orientation. Similar observation is made for the accumulated plastic strain map. One important feature from the accumulated plastic strain map is the extreme heterogeneity with locations experiencing very little plastic strain accumulation, and regions of accumulated plastic activity as high as 55%. Looking at the von Mises stress plot, it can be seen that there is much less heterogeneity, at least when compared to the strain plots. The von Mises stress scale begins at 800 MPa and even at this scale, not many regions can be seen to have such low stresses. Nonetheless, the von Mises stress seems to obey morphological constraints such as grains and grain boundaries, in contrast to other quantities. The same holds for the stress triaxiality plot. The map of the number of active slip systems is also given in Fig. 10. This variable ranges in principle from 1 to 12. However, it can be seen that the estimated number of activated slip systems does not reach such large values but mostly remains between 1 and 3. The plot shows that a value of 1 is observed mostly at the core of the

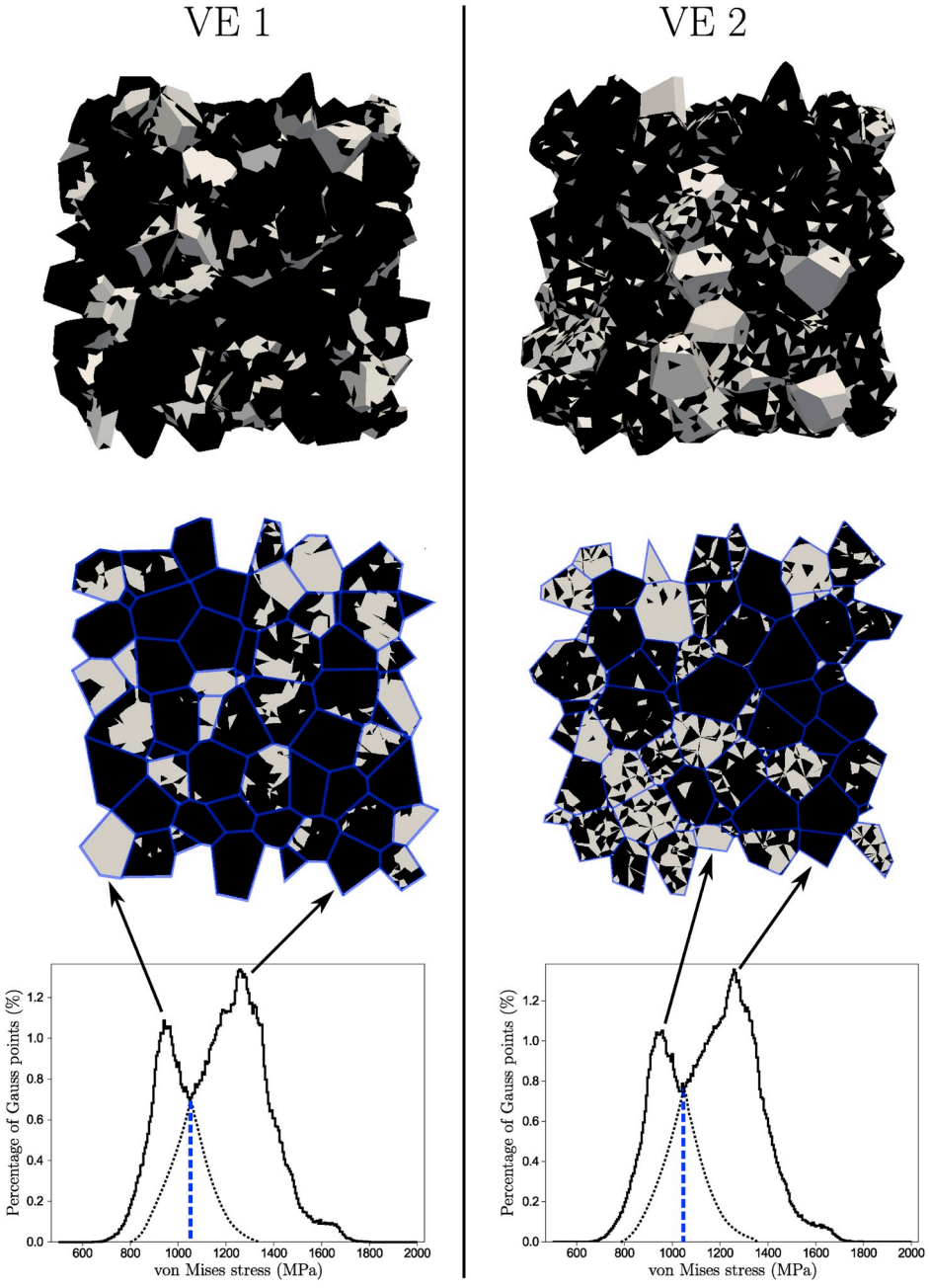

Fig. 13. For both VE 1 and 2, von Mises stress distribution at the tensile peak of the 100th cycle for $\Sigma_{11} = 1021$ MPa and $R_\Sigma = -0.7$. The distribution curve has been broken down into two parts and the associated regions are shown in the microstructure respectively. All Gauss points in the first part of the distribution curve are colored grey in the microstructure, while all Gauss points in the second part of the distribution curve are colored black.

grains where a single slip system is active. On the other hand, darker regions of the active slip system plot exist at the grain boundaries where different grains interact and multislip is likely. Lastly, two plots for the Schmid factors are provided in Fig. 10: the maximum axial Schmid factor $m_{\max}$ and the total axial Schmid factor m_{total}. A high value of $m_{\max}$ indicates that the grains are rather soft, meaning that they experience low stress values. No clear correlation can be seen between the $m_{\max}$ map and the previous stress and strain maps. In contrast, interesting observations can be made from the m_{total} map. The variable m_{total} is the sum of all Schmid factors for uniaxial tensile direction. This quantity, is another indicator of multislip activity. A clear correlation can be seen between the m_{total} map and the field of von Mises stress. Wherever there is a high value of the von Mises stress, m_{total} is low and vice versa.

5.1.1. Observation of local ratcheting phenomena

Up till now the series comparison test to detect ratcheting or shakedown has been applied to the macroscopic averaged results. In this section the test is applied to each element of the finite element mesh in order to detect local ratcheting phenomenon. In the VE, the elements which ratchet are then displayed in red while those which exhibit shakedown are shown in blue. For the application of this test, three simulations are selected from the asymmetric stress controlled batch (VE 1, parameter set LK) after running 100 cycles. All three have the same loading ratio of $R_\Sigma = -0.7$ while the maximum applied stress varies as follows:

1. $\Sigma_{11} = 849$ MPa, macroscopic shakedown, 1.9% of ratcheting volume
2. $\Sigma_{11} = 983$ MPa, macroscopic shakedown, 29.0% of ratcheting volume

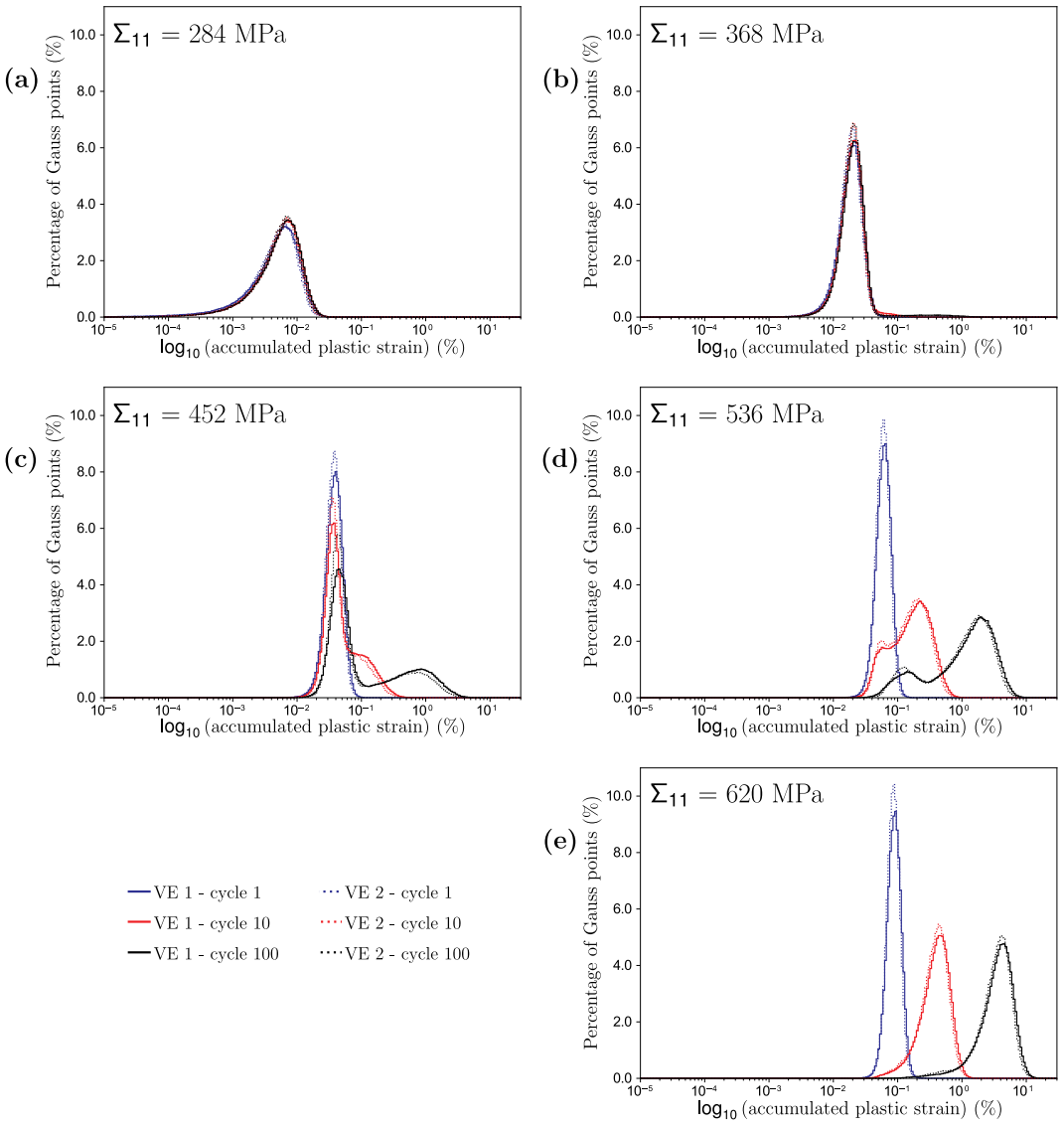

Fig. 14. Probability distribution curves for the accumulated plastic strain in five simulations with $R_\Sigma = 0$ and $\Sigma_{11} = 284$–620 MPa, using parameter set HK.

3. $\Sigma_{11} = 1021$ MPa, macroscopic ratcheting, 53.8% of ratcheting volume

Using the series comparison test for ratcheting and shakedown, the first two cases display macroscopic shakedown while the third exhibits macroscopic ratcheting. Fig. 11 elaborates this further where the three aforementioned cases are shown. The first line shows the whole VE. In the second line of the figure, only the finite elements of the volume which undergo ratcheting can be seen for all three loads. The third line shows a 2D slice with the ratcheting and shakedown regions. It seems that the regions that ratchet do not conform to grain morphology or any particular locations and are rather random in nature.

It can be seen that the ratcheting zones of the polycrystal tend to percolate to form a connected ratcheting domain when increasing the applied stress and before macroscopic ratcheting is observed. The volume fraction of the percolating ratcheting zone has been determined following the method proposed in Kanit et al. (2006) and was found to reach full percolation for the two higher loads illustrated in Fig. 11. In contrast, in the left column of Fig. 11 for lower load values, isolated islands of ratcheting are observed. No direct link could be derived between the corresponding percolation threshold and the occurrence of plastic shakedown or ratcheting.

5.1.2. Probability density distributions

Fig. 12 presents Gauss point distribution plots for $\Sigma_{11} = 1021$ MPa, and $R_\Sigma = -0.7$. Both VEs are considered: The solid line represents VE 1, while the dotted line represents VE 2. To show the evolution of each variable with respect to cycle number, the statistics are collected at the tension peak of cycles 1, 10 and 100. In Fig. 12(a), the histogram plot of von Mises stress shows a multi-modal distribution where the peaks can be seen to progressively split as the number of simulated cycles increases. This point will be analyzed in the next paragraph and in the next two figures. With regards to the accumulated plastic strain according to Fig. 12(c), it can be seen that for the first cycle, the distributions are first unimodal but as the cycle number increases, a hump is produced in the left part of the curves. This will be characterized later in this article. Looking at the von Mises strain distribution, it can be seen that, with an increase in the number of cycles, the curves translate along the strain axis, as a result of the ratcheting phenomenon. The standard deviation of von Mises strain is found to increase with the cycle number. Regarding the stress triaxiality, the standard deviation similarly increases with the cycle number. Lastly, the number of active slip systems can be seen to be less than six and with the progression of cycles, single slip starts to dominate. The representativity of the results is confirmed by the fact that all the dotted and solid lines corresponding to VE 1 and 2 are close to each other. An exception is the von Mises strain distribution plots for which slight deviations are observed, which shows a slightly different ratcheting intensity of each volume. The intensity of ratcheting surely is a very sensitive result of polycrystalline material response. More precise estimates would require the consideration of additional volume elements.

5.1.3. Evidence of bimodal stress distribution

As seen in Fig. 12, the von Mises stress probability distribution curves exhibit a multimodal distribution. This fact has already been observed by several authors using crystal plasticity simulations (Osipov et al., 2008; Schwartz et al., 2013; Lee et al., 2011; Choi et al., 2012). What is missing is a detailed analysis showing the origin of this phenomenon. Fig. 13 shows the von Mises stress distribution curve taken at the tensile peak of the 100th cycle for $\Sigma_{11} = 1021$ MPa and $R_\Sigma = -0.7$. Two distinct peaks can be seen in the distribution arbitrarily separated by a dashed line. This separation makes it possible to split the polycrystalline volume into two parts, the first (resp. second) one containing the Gauss point displaying a von Mises equivalent stress lower (resp. larger) than this separation value. The volume fractions in each peak are then shown in the 3D and 2D views of Fig. 13, with a grey (resp. black) color corresponding to the first (resp. second) peak. It can be noted that the black and grey regions contain mostly full grains, i.e. each grain is either completely black or grey. Of course there are some exceptions where some grains are split into grey and black zones. They reflect the fact that the distribution curve of von Mises stress was split arbitrarily and the region between the two black dotted lines in the histogram of Fig. 13 has overlapping points. The observation of the total axial Schmid factors plot of Fig. 10 indicates that the black regions correspond to hard grains,

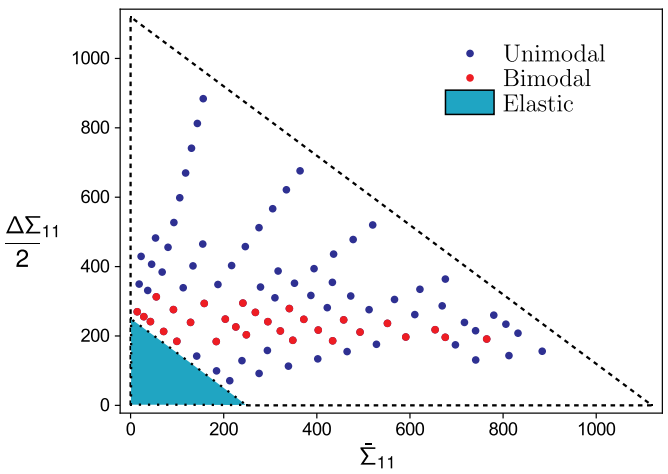

Fig. 15. Modality diagram for parameter set HK, VE 1. It characterizes the existence of unimodal or bimodal distributions of accumulated plastic strain.

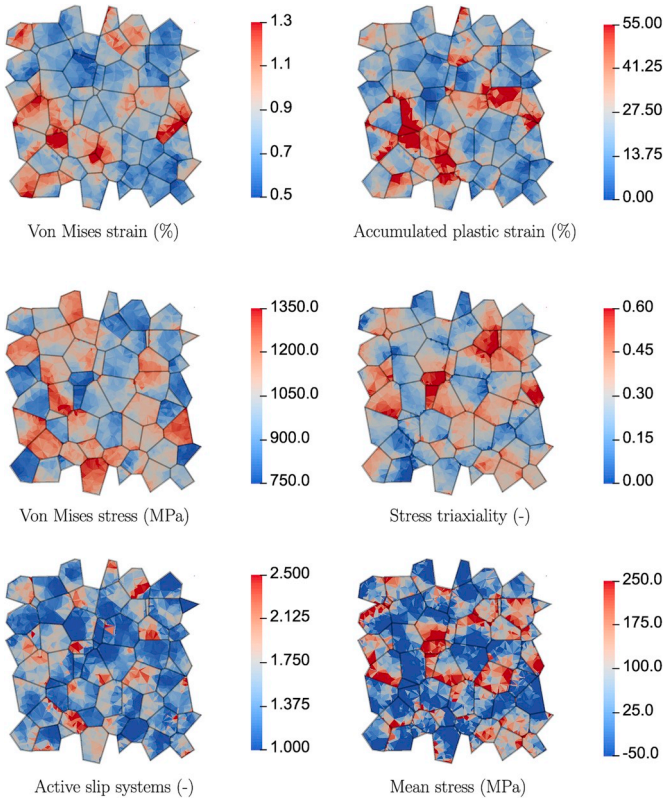

Fig. 16. Contour plots of a simulation with asymmetric strain of $E_{11} = 0.85\%$ and $R_E = -0.2$ after running one hundred cycles, extracted at the maximum strain of the one hundredth cycle (VE 1, parameter set LK). The contour plots show the von Mises strain, accumulated plastic strain, von Mises stress, stress triaxiality, maximum slip divided by total slip, and the local mean stress.

and the grey regions correspond to soft grains. It is concluded that the polycrystal aggregate progressively splits into main regions of high and low stresses strongly correlated with the hard/soft character of the grains.

5.1.4. Evidence of bimodal accumulated plastic strain distribution

Bimodality is also observed in the distribution of accumulated plastic strain or accumulated slip in Fig. 12(c and d), when the number of simulated cycles increases. This is not always the case. Fig. 14 shows the Gauss point results from five simulations. These simulations pertain to parameter set HK, $\Sigma_{11} = 284$, 368, 452, 536, 620 MPa, and $R_\Sigma = 0$. The trend that can be seen in log accumulated plastic strain plot distribution curves is that the first and last plots ($\Sigma_{11} = 284$ and 620 MPa) are unimodal regardless of the number of simulated cycles while the other three plots start with one peak and then split into two peaks. This bimodality reveals the existence of two regions that develop inside the polycrystal: A first one where elastic or plastic shakedown occurs and the second where ratcheting takes place. It can also be seen that the volume of these regions depends on the applied load.

Most importantly, it is noted that this bimodality does not always arise depending on loading values. It is therefore possible to draw a map of the existence domain of bimodal accumulated plastic strain distribution depending on the applied stress amplitude and mean stress. This is done in Fig. 15 taking the already performed simulations for VE 1 and parameter set HK. The obtained modality diagram of Fig. 15 can be compared to the ratcheting diagram of Fig. 5 based on the series criterion. It is remarkable that the domain of bimodality is found to almost coincide with the domain of plastic shakedown. This major finding suggests that stable bimodal plastic strain distributions correspond to a transition regime between shakedown (elastic or plastic) and ratcheting material response. This feature can be also be used as a criterion for the detection of plastic shakedown replacing or in addition to the series convergence criterion. This conclusion is confirmed by the results of VE 2 (modality map not provided here for conciseness). Note that the distribution of equivalent plastic strain is not bimodal. It looks rather very similar to the von Mises strain distribution plots.

5.2. Mean stress relaxation

The analysis of the local results must also be performed for other loading conditions. Such an analysis is performed in this section in the case of strain controlled tests in order to characterize some microstructural features associated with mean stress relaxation. For the next three figures a strain controlled simulation for VE 1 with parameter set LK and $R_E = -0.2$ and $E_{11} = 0.85\%$ is considered. The results plotted pertain to the tensile peak of the 100th cycle. The contour plots of Fig. 16 can be compared with those of Fig. 10 (a) (stress controlled compared to strain controlled). It can be seen that both are very similar. In particular, the map of the von Mises strain shows

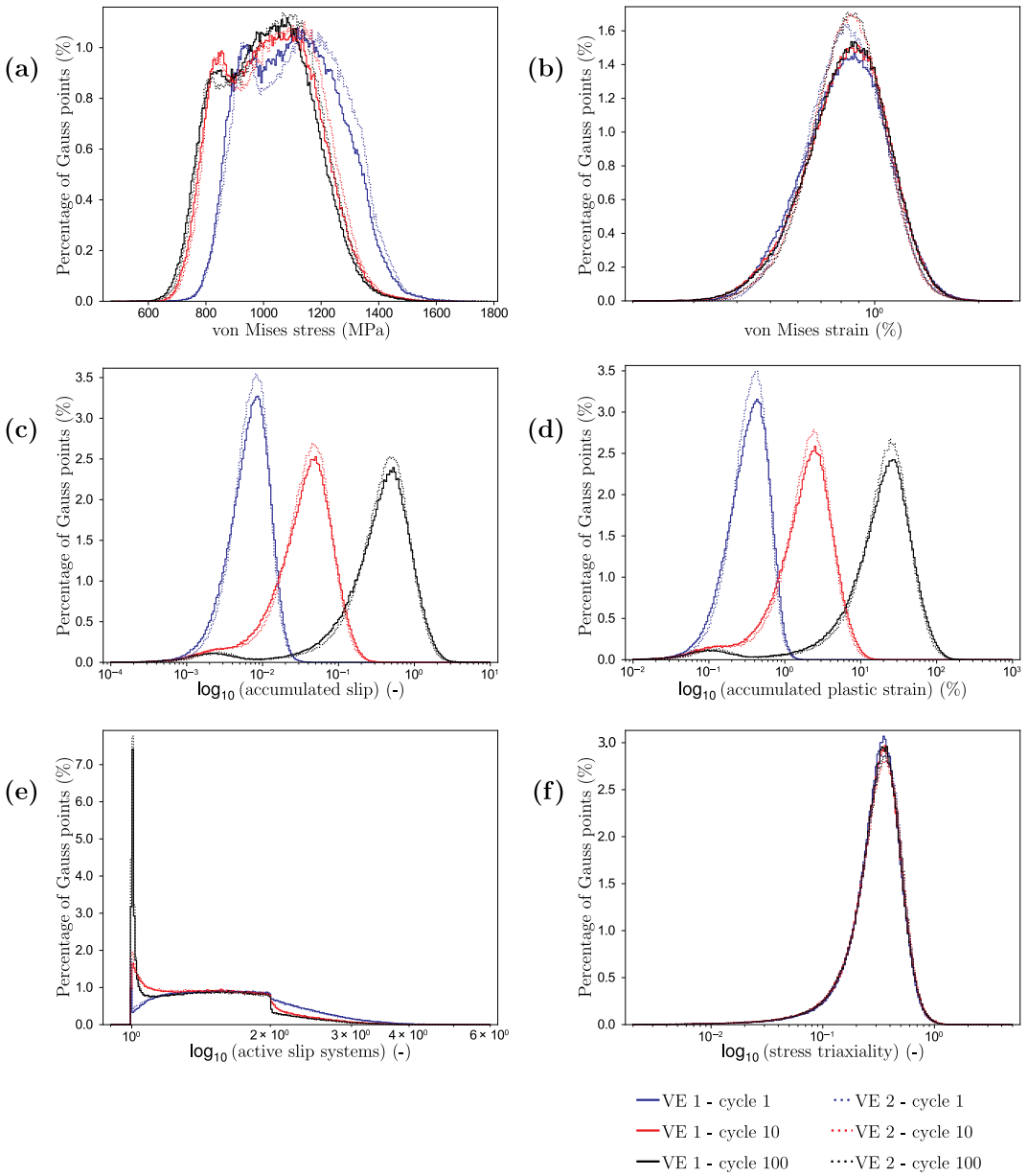

Fig. 17. Distribution curves of Gauss point variables for an asymmetric strain controlled test using parameter set LK, $R_E = -0.2$ and $E_{11} = 0.85\%$. The variables shown are (a) von Mises stress (b) von Mises strain, (c) accumulated slip, (d) accumulated plastic strain, and (e) stress triaxiality.

that the most deformed grains are almost the same for both simulations, except that the strain controlled simulation leads to much lower strain values. The following definition of a local mean stress is proposed:

$$((\sigma^t_{11} + \sigma^t_{22} + \sigma^t_{33}) + (\sigma^c_{11} + \sigma^c_{22} + \sigma^c_{33}))/2 \tag{21}$$

where the subscripts t ans c indicate that the variables were collected at the macroscopic tensile or compressive peak of their cycle. The observation of the mean stress plot indicates that it segregates at the grain boundaries or at triple junctions, and is less prone to be high within the grains. It is hypothesized that this intergranular interaction prevents the mean stress from relaxing to zero in a polycrystal.

The distribution curves for Gauss point variables are plotted in Fig. 17. The solid lines represent VE 1 while dotted lines represent VE 2. Both VEs exhibit a matching response which signifies good representativity of the material. The von Mises stress plot shows the distributions curves translating back on the stress axis which reflects the decrease of the average mean stress per cycle. Again, multi-modality is observed for the strain based loading conditions as it was observed for stress control in the previous section with regards to ratcheting. Von Mises strain and stress triaxiality plots display somewhat similar distributions. The plot of the number of active slips systems indicates that single slip gets more dominant as the number of cycles increases. Accumulated slip and accumulated plastic

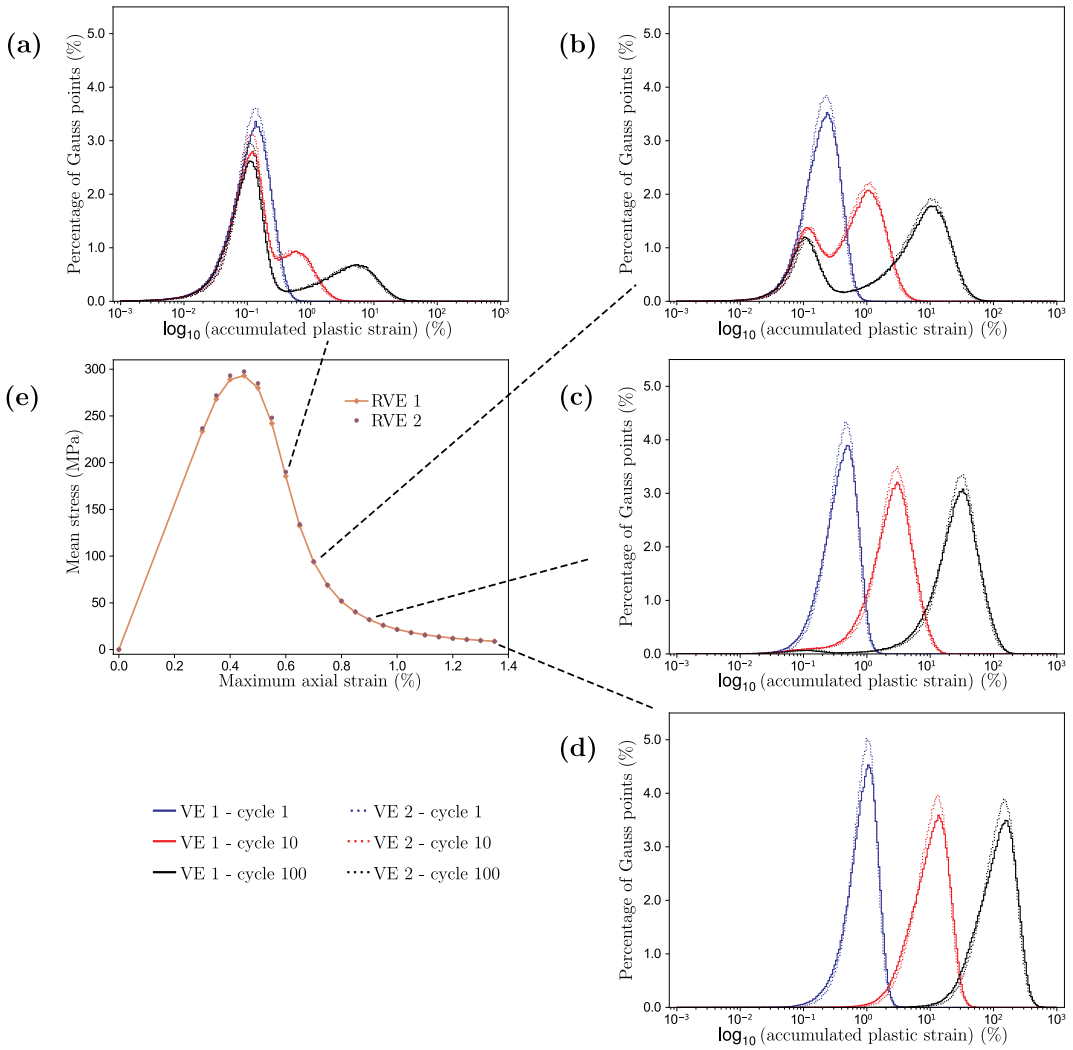

Fig. 18. For VE 1 and 2, parameter set LK, distribution curves for the accumulated plastic strain per Gauss point for four maximum axial strain values. (a), (b) and (c) show a bimodal while (d) shows a unimodal distribution. (e) gives the mean stress for different maximum axial strains at cycle 100.

strain exhibit bimodal distributions as in the stress controlled case. The next figure sheds some light on the development of bimodality in the context of mean stress relaxation test. Fig. 18 shows the breakdown of bimodality in accumulated plastic strain for parameter set LK, VE 1 and 2. It can be seen that for the first two cases (a) and (b), the curves start as a unimodal distribution but then split into bimodal distributions. Just like in the stress controlled case, these curves indicate that a hundred cycles are not enough to reach a saturated response, as the bimodal peaks are still splitting. The two peaks that form imply that the microstructure splits into two regions, one in which plastic activity stops after some cycles (the first stagnant peak), and the other accommodating all plastic deformation (the second peak which keeps moving forward). At high strains, as shown in Fig. 18 (d), the whole microstructure undergoes plastic activity resulting in a unimodal distribution. It is hypothesized from the present observations that when the plasticity distribution becomes unimodal, mean stress will relax to zero.

6. Simulations at high cycle numbers

The previous observations have been made from the hundred cycle response of the polycrystalline aggregates. The objective of this last section is to check the validity of the drawn conclusions at higher cycle numbers. Using crystal plasticity for low cycle fatigue, some authors have already simulated thousands of cycles (Joseph et al., 2010; Zhang et al., 2015), but the results provided here for the first time pertain to a finely meshed polycrystal aggregate under asymmetric loading conditions. The mesh is fine enough to provide detailed distribution of local stress and strain fields as illustrated in the previous sections. For instance the present finite element meshes contain almost 600000 degrees of freedom for 300 grains to be compared with 150000 d.o.f. and 250 grains considered by Colas et al., 2019 where more than 1000 cycles were simulated. Two cases are reported in this section where the first case pertains to

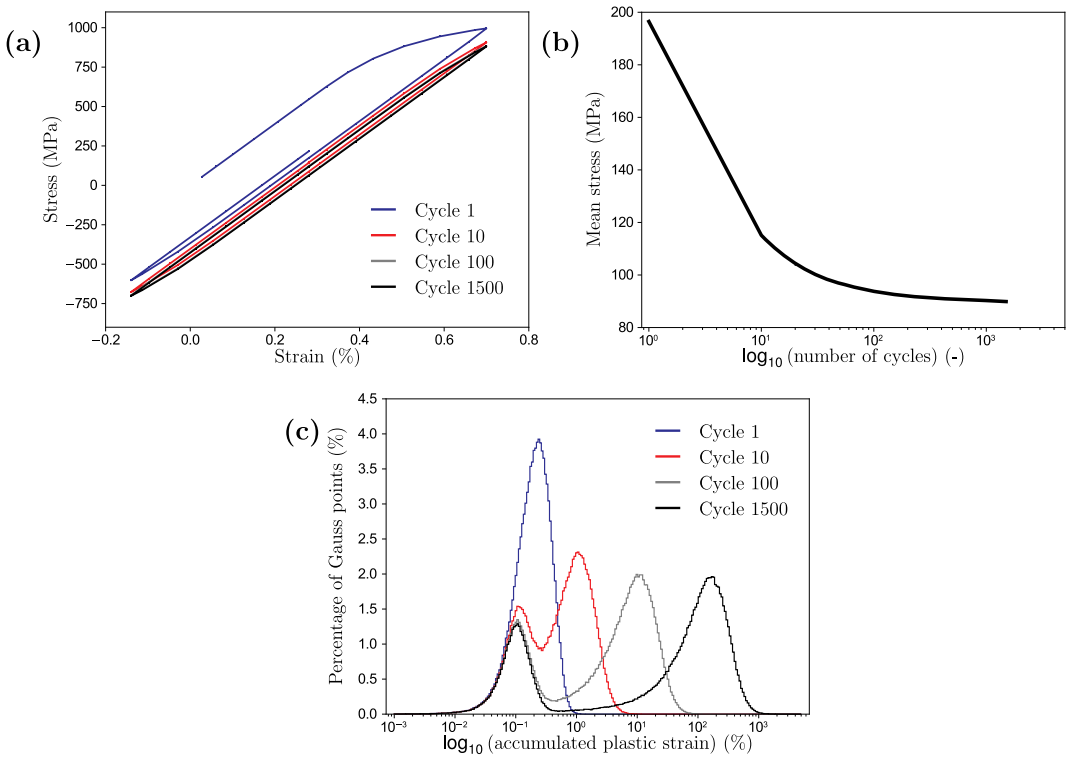

Fig. 19. Long cyclic simulation with asymmetric strain controlled boundary conditions for VE 1, parameter set LK: $E_{11} = 0.7\%$, $R_E = -0.2$. (a) The stress strain hysteresis loops for cycles 1, 10, 100 and 1500. (b) Macroscopic mean stress plotted against the number of cycles. (c) Gauss point distribution of the accumulated plastic strain for different cycles.

one simulation on VE 1 under asymmetric strain controlled periodic boundary conditions with $R_E = -0.2$, and $E_{11} = 0.7\%$ run for 1500 cycles. Fig. 19 (a) and (b) illustrate the global mean stress relaxation over the 1500 cycles. It can be seen that the cyclic mean stress does not relax to zero even after 1500 cycles, and seems to have reached a saturated value signified by the saturating curve of mean stress in (b). The accumulated plastic strain plot of Fig. 19 (c) further confirms the bimodal distribution with one part of the aggregate experiencing further plastic activity whereas the first peak corresponds to an elastically accommodated region of the crystal. The same trend was observed after 100 cycles and is continuing further after 1500 cycles.

It is instructive to compare the obtained results with a simulation involving a larger number of grains at the expense of a coarse mesh. The objective is to confirm the representativity of the presented results even though this feature was supported by the consideration of VE 1 and 2. A new VE with $15^3 = 3375$ grains and with one single hexahedral quadratic element per grain is generated, see Fig. 20(a). Using parameter set LK, asymmetric periodic strain loading of 0.6% and $R_E = -0.2$ is imposed. The simulation is run for 6000 cycles. Fig. 20(b) shows the macroscopic stress strain response while (c) shows the accumulated plastic strain at the first, hundredth and six thousandth cycles. It can be seen that the macroscopic stress strain response does not change from the hundredth to the thousandth cycle but the accumulated slip has the same bimodal response as observed in the previous simulations. Just as before, the microstructure divides into two distinct regions: one that stops accumulating plasticity, and the other which takes all the plastic deformation indicating that these results are consistent with the study presented in this paper.

7. Discussion

The motivation of the present work is to show the capabilities of the crystal plasticity model to reproduce the types of asymmetric cyclic responses observed for engineering metallic materials. The contents of the work are therefore of computational nature and experimental confirmation of some evidenced phenomena, like statistical distributions of field variables is an open question. The objective of the present work is not to match macroscopic curves for a particular material but to prove that the different experimentally observed regimes, namely ratcheting, elastic shakedown, plastic shakedown, and a complete or incomplete mean stress relaxation, are properly accounted for by full field polycrystal simulations. The simulation results are now discussed with respect to experimental evidence from the literature.

Regarding asymmetric stress controlled simulations, Fig. 5 illustrates different cyclic regimes experienced by polycrystals. These regimes i.e. ratcheting, plastic shakedown and elastic shakedown, depend on the applied stress amplitude and mean stress. For 316 stainless steels Pellissier-Tanon et al. (1982) have presented experimental evidence for plastic shakedown and ratcheting. Similarly, with an increasing mean stress, Park et al. (2007) present experimental data for ratcheting in Inconel 718, and Lim et al. (2009); Das

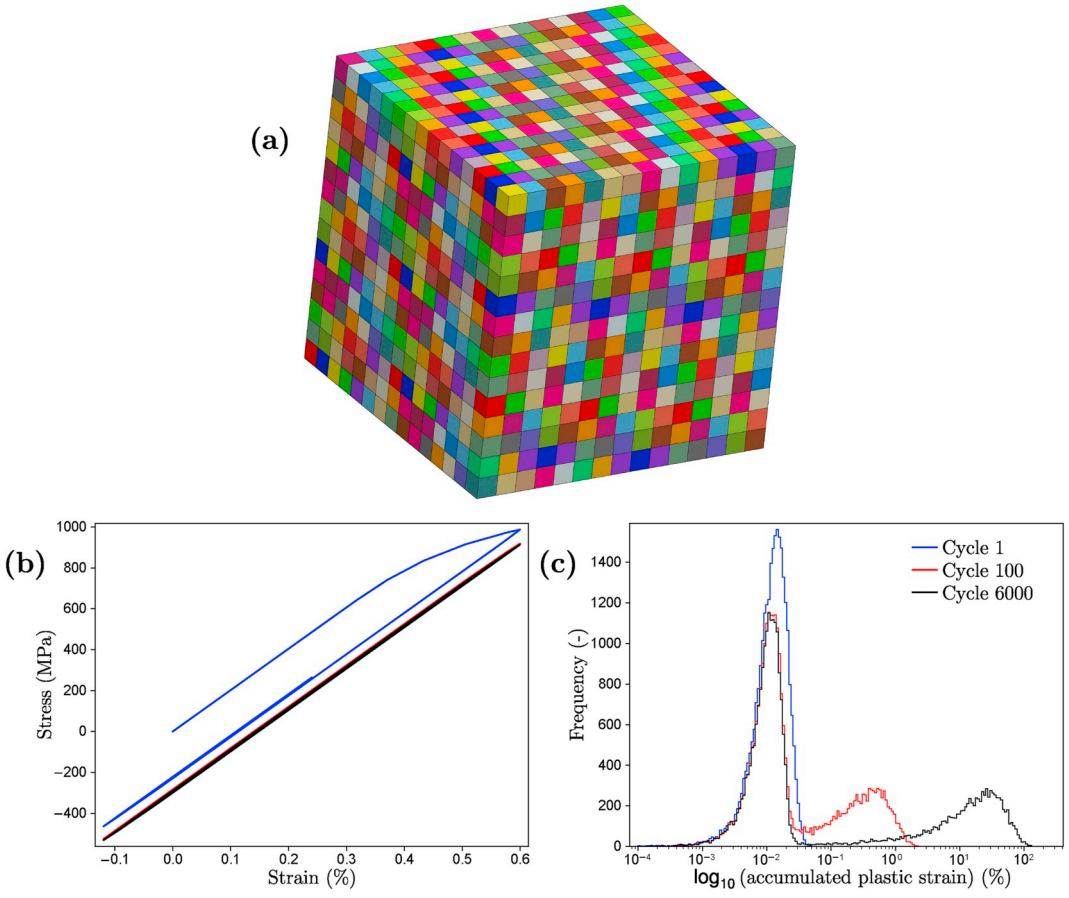

Fig. 20. Using asymmetric strain controlled boundary conditions, with $E_{11} = 0.6\%$ and $R_E = -0.2$ and parameter set LK: (a) a coarse meshed volume element with 3375 grains and one quadratic element per grain, (b) The macroscopic stress vs strain loops for cycles 1, 100 and 6000. (c) Accumulated plastic strain after the three cyclic instances.

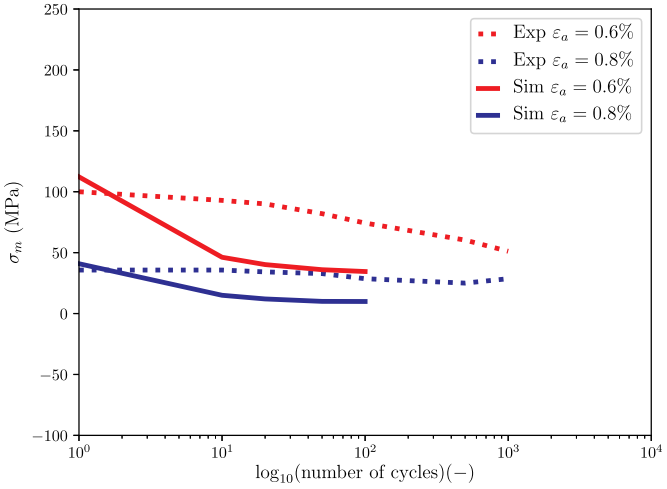

Fig. 21. Using asymmetric strain controlled tests, evolution of mean stress for two different strain amplitudes: $\varepsilon_a = 0.6$ and 0.8%. Simulation are presented with solid lines while experiments are shown with dotted lines. The experimental curves are taken from Gribbin et al. (2016).

and Chakraborti (2011) for ratcheting in copper. For 316 and 304 steels, an important feature found by Goodman (1984) and recently Taleb and Keller (2018), is that increasing the stress amplitude under a constant non-zero mean stress or increasing the applied mean stress under a given stress amplitude, both increase the rate of ratcheting. Fig. 5 in the present article numerically characterizes these complex cyclic phenomena and gives an insight of how a little variation in the applied stress can result in a switch between shakedown

and ratcheting.

In contrast, under asymmetric strain controlled loadings, depending on the applied strain amplitude, experiments usually exhibit a non-zero cyclic mean stress. For Inconel 718, this has been demonstrated experimentally by Prithivirajan and Sangid (2018); Gribbin et al. (2016) whereas for steels Wehner and Fatemi (1991); Nikulin et al. (2019) have reported such behavior. In addition, asymmetric strain controlled experiments show that the mean stress relaxes to progressively lower values with an increasing strain amplitude as found for Inconel 718 by Chaboche et al. (2012) and aluminum by Hao et al. (2015). Figs. 7 and 8 show a qualitative replication of such behaviors where increasing the applied strain amplitude leads to smooth decreasing of mean stress until complete relaxation. Using literature findings to validate the qualitative results on mean stress relaxation, two simulations were run using parameter set LK and compared with the experimental data reported by Gribbin et al. (2016) for Inconel 718. The plots of Fig. 21 show that the full field polycrystal simulations predict non complete stress relaxation as observed in the corresponding experiments. The model however overestimates the amount of stress relaxation. A calibration of the parameters to the IN718 behavior is necessary to deliver more precise predictions.

After establishing that the crystal plasticity model can reproduce generic macroscopic responses, the next step is to check what happens inside the microstructure at the grain scale. The motivation behind this scrutiny is that full field crystal plasticity simulations are known to predict strong local strain heterogeneities induced by incompatibilities at grain boundaries (Barbe et al., 2001). Some authors have already been able to model asymmetric cyclic responses using mean-field homogenization models like the self-consistent scheme (Krishna et al., 2009; Sai and Cailletaud, 2007; Zecevic and Knezevic, 2018; Zecevic et al., 2016). In addition to that, full field simulations also provide local heterogeneities that play an essential role in fatigue crack initiation.

At the local level, two types of simulation results were presented, namely contour maps as well as probability distribution plots of several constitutive variables. For intragranular strain localization several experimental observations are available either using in-situ SEM DIC (Stinville et al., 2016; Stein et al., 2014; Zhao et al., 2008a; Walley et al., 2012), or for sub-grain strain fields (Di Gioacchino and Quinta da Fonseca, 2013; Kammers and Daly, 2013). These findings though important are mostly reported after applying monotonic tensile loadings. Measurements by Abuzaid et al. (2012) reveal the experimental distribution of the accumulated plastic strain after a monotonic tensile load. A major finding of our simulations is that under asymmetric cyclic loads, the accumulated plastic strain splits into a bimodal distribution, see Figs. 12 and 17. It must be noted also that the distribution curves in the present paper pertain to the bulk of the polycrystal whereas experimental findings usually adhere to surface measurements. Interestingly, crack size distributions in a nickel-based superalloy under HCF loading conditions were experimentally determined by Shenoy et al. (2007). Such damage distributions can be correlated with the distribution of Fatigue Indicator Parameters directly linked to plastic activity in the grains. However, such papers deal with symmetric loading conditions which also in computations result in a unimodal plastic strain distribution. To this extent, no experimental evidence of bimodal strain distributions has been found in literature. It is hoped that the new features of plastic behavior found in the present study will give incentives for future experimental works including strain field measurements for non-symmetric cyclic loading conditions.

8. Conclusions

Using rate-independent crystal plasticity with kinematic hardening, the cyclic response of FCC polycrystalline materials has been characterized both at the macroscopic and local levels. The macroscopic response was summarized by appropriate mean stress/stress amplitude maps whereas the mechanisms underlying each type of material response were explored using local statistics. Two sets of materials parameters with various amounts of yield stress and hardening were considered in order to illustrate the capability of the polycrystal model to capture complex loading behavior under strain or stress loading control. All simulations were run for a hundred cycles each, and more than 1000 cycles for some of them, and then the response was analyzed. The single crystal material model was kept as simple as possible because it is sufficient to explain, at least qualitatively, most features of the observed polycrystal behavior. Evaluation of the results reveals the following major findings:

- For stress controlled asymmetric simulations:
  1. Strain ratcheting in a single (resp. poly) crystal is characterized by three (resp. four) regimes. Elastic accommodation and ratcheting regimes are common to single and polycrystals. In contrast, plastic shakedown takes place only in polycrystals.
  2. A series comparison test as well as the bimodality of accumulated plastic strain distribution criterion were proposed to detect ratcheting or plastic shakedown. A remarkable result of the analysis is the evidence of a correlation between the existence of a bimodal distribution and overall plastic shakedown.
  3. A theoretical diagram for ratcheting in single crystals is built in terms of the stress amplitude versus mean stress. Several simulations were run and a similar diagram was filled for the polycrystal showing different regimes of elastic and plastic shakedown as well as ratcheting.
  4. Gauss point statistics indicate that the von Mises stress in polycrystals is bimodal. These two modes become more prominent under progressive cyclic loading and they correspond to different regions of the polycrystal respectively made of soft and hard grains in the sense of Schmid factor.
  5. Local ratcheting events were observed in polycrystals experiencing plastic shakedown at the macroscopic scale.
  6. Evolution of the number of activated slip systems during cycling shows a trend towards single slip occurring in the core of the grains while multislip is observed mostly at grain boundaries.
- For strain controlled asymmetric simulations:

1. Cyclic mean stress relaxation in a single crystal can be broken down into three distinct regimes: Purely elastic response, elastic accommodation after a first elastoplastic period and plastic shakedown with vanishing mean stress. Instead, in a polycrystal, a smooth transition between these scenarios is observed. Mean stress relaxation towards stabilized finite values was observed for polycrystals.
2. Cyclic mean stress relaxes to near zero for parameter set HK (high kinematic hardening), whereas it does not relax to zero for parameter set LK (high yield strength).
3. Distribution curves of the accumulated plastic strain are found to be bimodal under some loading conditions. One part of the microstructure undergoes purely elastic accommodation whereas the remaining part of the polycrystal experiences continuing plastic activity. From these observations, it is conjectured that the mean stress in a polycrystal will relax to zero when the distribution becomes unimodal.
4. Contour plots reveal that the high cyclic mean stress is more susceptible to segregate at grain boundaries or at triple junctions and this local interaction causes a nonzero mean stress in a polycrystal.

These results show that the grain to grain interactions induce cyclic responses that strongly differ from that of the single crystal. In particular these interactions are responsible for the existence of plastic shakedown regimes under stress control and of incomplete mean stress relaxation under strain control. This work contributes to the understanding of complex stress-strain redistribution phenomena at work in cyclically loaded polycrystals using standard crystal plasticity models. These crystal plasticity models are uses extensively and their capability to mimic real polycrystals has been scrutinized in this article. The macroscopic responses of both stress and strain controlled tests are in good agreement with experimental results for engineering FCC alloys where a plastic shakedown as well as a non-zero mean stress are frequently observed, for example in nickel-based superalloys. It remains that the present work is limited to computational analyses and should serve as an incentive for experimental observations of the evidenced features of asymmetric cyclic plasticity in FCC polycrystalline aggregates.

Other methods of statistical analysis could be used to dig into the huge amount of data produced in this work. Machine learning techniques have also been used in recent works to find out some meta-models for fatigue crack initiation. The potential of such methods is considered by Rovinelli et al. (2014) to predict the initiation of small fatigue cracks in polycrystals.

The current ongoing work compares the presented results with both the predictions from mean field polycrystal models and those from multiaxial macroscopic loading conditions. Consideration of rate-dependence in future simulations could shed some light on the cyclic-creep behavior of alloys at higher temperatures (Taleb and Keller, 2018). The evidence of local ratcheting in the complex simulated fields can be used to define fatigue indicator for damage initiation (Pécheur et al., 2012; Lu et al., 2014; Colas et al., 2019).

Acknowledgments

The authors gratefully acknowledge the financial support of *Chaire Cristal* with SafranTech. They also thank Tonya Rose and Arjen Roos from SafranTech for fruitful scientific discussions of the work and careful reading of the manuscript.

Appendix A. Analysis of mesh sensitivity

Selecting the appropriate mesh density for finite element polycrystal simulations is not straightforward. A start can be taken by refining the mesh until a converged macroscopic tensile curve is obtained but finding macroscopic properties is not the only goal of the work. If macroscopic properties were the main goal, then macroscopic models could have been used or even mean field models which take into account a lot of local information and are much faster to perform as well as require considerably less computational resources. The goal here is also to assess local responses inside the grains. This requires large number of degrees of freedom in each grain. Also there is considerable difference in the solutions obtained using different boundary conditions. In this article two types of boundary conditions are used: Periodic strain control or periodic stress control. Periodic stress boundary conditions are anticipated to produce more convergence issues as compared to periodic strain because in metal plasticity, a small increment in stress produces a large increment in strain. This effect is even more pronounced at the local level because of severe heterogeneity in crystal plasticity simulations. With regards to VE 1 which contains 300 grains, three mesh densities were tested for this paper:

1. Coarse mesh with 112565 nodes and 74270 quadratic elements
2. Mesh in use with 194903 nodes and 130171 quadratic elements
3. fine mesh with 270670 nodes and 181905 quadratic elements

A tensile test on these meshes was performed and three responses were compared i.e. the macroscopic averaged stress strain response, the von Mises equivalent stress and strain at each Gauss point at the maximum traction/displacement. For periodic strain control a 2% macroscopic strain was imposed while for periodic stress a macroscopic stress of 1110 MPa was imposed in the tensile direction. Figs. 22 and 23 Figure 22Figure 23 show the three responses for both loading conditions. For strain controlled loading, all three meshes provide a somewhat converged solution, both at the macroscopic level and at the local level. Apart from some mismatch in the local von Mises stress distribution curve there even the coarse mesh seems to do the job. This is not the case for stress based loading conditions. At the macroscopic scale, the three meshes do not lead to the same value of the mean strain at the final loading point, see Fig. 23(a). The largest discrepancies are found for the equivalent stress distribution, Fig. 23(b). This shows that load controlled asymmetric simulations require a very fine mesh to obtain converged local strain distributions. Also, even if there is a small

error in the applied stress at each increment, it can result in a significant error in the calculated strains. Using 24 parallel cores for each job, the time needed to run one tensile load controlled test on each mesh was 10, 33 and 60 h respectively. Although differences can be observed in the load controlled simulation, hundreds of tests were required for this study and hence the intermediate mesh size with 130171 elements was selected.

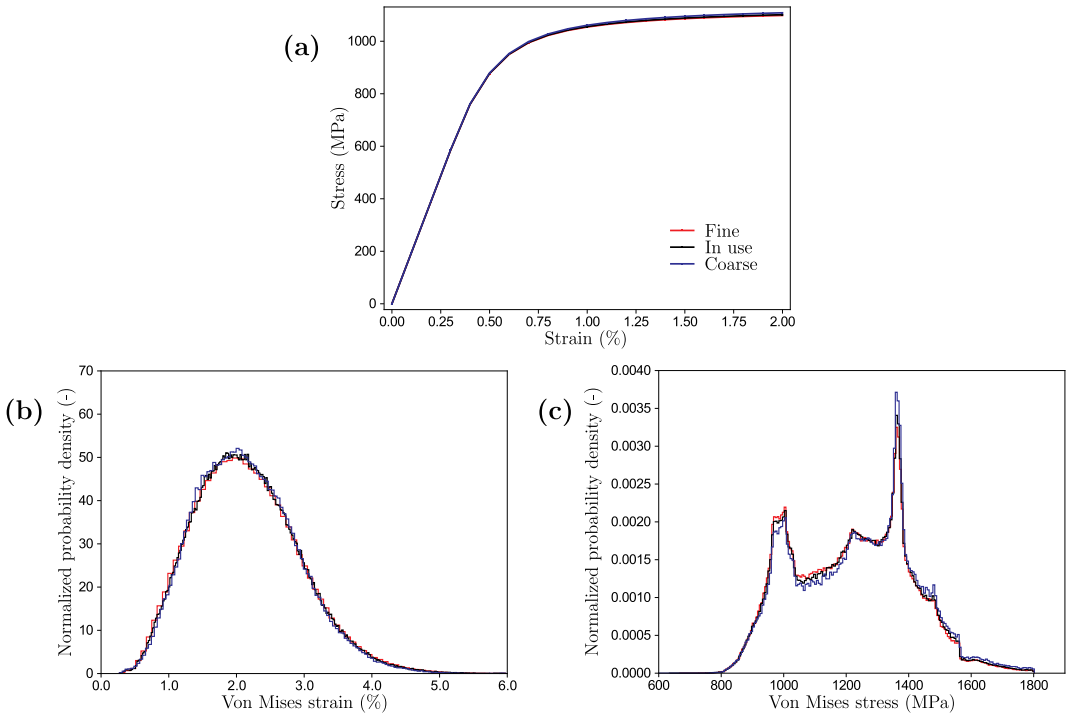

Fig. 22. Using parameter set LK, tensile test simulations for three finite element meshes under a macroscopic periodic strain of 2%: (a) macroscopic averaged stress strain plot,(b) and (c) von Mises equivalent strain and stress distributions at the peak macroscopic strain.

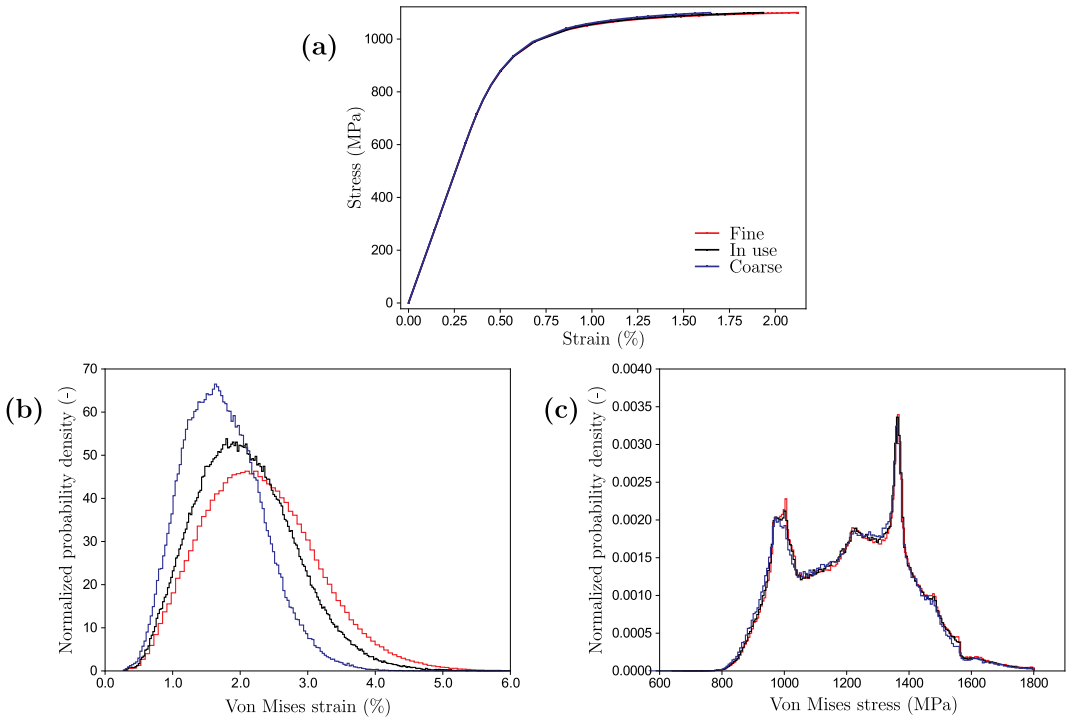

Fig. 23. Using parameter set LK, tensile test simulations for three finite element meshes under a macroscopic periodic load of 1100 MPa: (a) macroscopic averaged stress strain plot, (b) and (c) show the von Mises equivalent strain and stress at the peak macroscopic stress.

Appendix A. Supplementary data

Supplementary data to this article can be found online at https://doi.org/10.1016/j.ijplas.2019.10.007.

References

Abuzaid, W.Z., Sangid, M.D., Carroll, J.D., Sehitoglu, H., Lambros, J., 2012. Slip transfer and plastic strain accumulation across grain boundaries in hastelloy x. J. Mech. Phys. Solids 60, 1201–1220.

Arcari, A., Vita, R.D., Dowling, N.E., 2009. Mean stress relaxation during cyclic straining of high strength aluminum alloys. Int. J. Fatigue 31, 1742–1750.

Azzouz, F., Cailletaud, G., Chaboche, J.L., Ostoja-Kuczynski, E., Quilici, S., 2010. Cyclic calculations and life estimation in thermomechanical fatigue. 9th International Conference on Multiaxial Fatigue and Fracture, pp. 785–793.

Barbe, F., Forest, S., Cailletaud, G., 2001. Intergranular and intragranular behavior of polycrystalline aggregates. Part 2: Results. Int. J. Plast. 17, 537–563.

Besson, J., Cailletaud, G., Chaboche, J.L., Forest, S., Blétry, M., 2009. Non–Linear Mechanics of Materials. Solid Mechanics and its Applications, vol 167. Springer-Verlag Berlin Heidelberg. https://doi.org/10.1007/978-90-481-3356-7.

Bouchedjra, M., Kanit, T., Boulemia, C., Amrouche, A., Belouchrani, M.E.A., 2018. Determination of the RVE size for polycrystal metals to predict monotonic and cyclic elastoplastic behavior: statistical and numerical approach with new criteria. Eur. J. Mech. A Solid. 72, 1–15.

Busso, E.P., Cailletaud, G., 2005. On the selection of active slip systems in crystal plasticity. Int. J. Plast. 21, 2212–2231 (Plasticity of Heterogeneous Materials).

Chaboche, J., 1986. Time-independent constitutive theories for cyclic plasticity. Int. J. Plast. 2, 149–188.

Chaboche, J., 1989. Constitutive equations for cyclic plasticity and cyclic viscoplasticity. Int. J. Plast. 5, 247–302.

Chaboche, J.L., Kanouté, P., Azzouz, F., 2012. Cyclic inelastic constitutive equations and their impact on the fatigue life predictions. Int. J. Plast. 35, 44–66.

Choi, Y., Groeber, M., Turner, T., Dimiduk, D., Woodward, C., Uchic, M., Parthasarathy, T., 2012. A crystal-plasticity FEM study on effects of simplified grain representation and mesh types on mesoscopic plasticity heterogeneities. Mater. Sci. Eng., A 553, 37–44.

Colas, D., Finot, E., Flouriot, S., Forest, S., Mazière, M., Paris, T., 2019. Local ratcheting phenomena in the cyclic behavior of polycrystalline tantalum. JOM J. Miner. Metals Mater. Soc. 71, 2586–2599.

Cruzado, A., LLorca, J., Segurado, J., 2017. Modeling cyclic deformation of Inconel 718 superalloy by means of crystal plasticity and computational homogenization. Int. J. Solids Struct. 122–123, 148–161.

Cruzado, A., Urchegui, M., Gómez, X., 2012. Finite element modeling and experimental validation of fretting wear scars in thin steel wires. Wear 289, 26–38.

Das, D., Chakraborti, P., 2011. Effect of stress parameters on ratcheting deformation stages of polycrystalline ofhc copper. Fatigue Fract. Eng. Mater. Struct. 34, 734–742.

Di Gioacchino, F., Quinta da Fonseca, J., 2013. Plastic strain mapping with sub-micron resolution using digital image correlation. Exp. Mech. 53, 743–754.

Dingreville, R., Battaile, C.C., Brewer, L.N., Holm, E.A., Boyce, B.L., 2010. The effect of microstructural representation on simulations of microplastic ratcheting. Int. J. Plast. 26, 617–633.

Dunne, F., Wilkinson, A., Allen, R., 2007. Experimental and computational studies of low cycle fatigue crack nucleation in a polycrystal. Int. J. Plast. 23, 273–295.

Forest, S., Rubin, M., 2016. A rate-independent crystal plasticity model with a smooth elastic–plastic transition and no slip indeterminacy. Eur. J. Mech. A Solid. 55, 278–288.

Fournier, D., Pineau, A., 1977. Low cycle fatigue behavior of Inconel 718 at 298 K and 823 K. Metall. Trans. A 8, 1095–1105.

Frederick, C., Armstrong, P., 2007. A mathematical representation of the multiaxial Bauschinger effect. Mater. A. T. High. Temp. 24, 1–26.

Ghorbanpour, S., Zecevic, M., Kumar, A., Jahedi, M., Bicknell, J., Jorgensen, L., Beyerlein, I.J., Knezevic, M., 2017. A crystal plasticity model incorporating the effects of precipitates in superalloys: application to tensile, compressive, and cyclic deformation of Inconel 718. Int. J. Plast. 99, 162–185.

Goodman, A., 1984. Development of constitutive equations for computer analysis of stainless steel components. Nucl. Eng. Des. 83, 349–354.

Gribbin, S., Bicknell, J., Jorgensen, L., Tsukrov, I., Knezevic, M., 2016. Low cycle fatigue behavior of direct metal laser sintered Inconel alloy 718. Int. J. Fatigue 93, 156–167.

Guilhem, Y., Basseville, S., Curtit, F., Stéphan, J.M., Cailletaud, G., 2018. Numerical analysis of the effect of surface roughness on mechanical fields in polycrystalline aggregates. Model. Simul. Mater. Sci. Eng. 26, 045004.

Hao, H., Ye, D., Chen, Y., Feng, M., Liu, J., 2015. A study on the mean stress relaxation behavior of 2124-T851 aluminum alloy during low-cycle fatigue at different strain ratios. Mater. Des. 67, 272–279.

Hassan, T., Kyriakides, S., 1994a. Ratcheting of cyclically hardening and softening materials: I. uniaxial behavior. Int. J. Plast. 10, 149–184.

Hassan, T., Kyriakides, S., 1994b. Ratcheting of cyclically hardening and softening materials: II. multiaxial behavior. Int. J. Plast. 10, 185–212.

Hennessey, C., Castelluccio, G.M., McDowell, D.L., 2017. Sensitivity of polycrystal plasticity to slip system kinematic hardening laws for Al 7075-T6. Mater. Sci. Eng., A 687, 241–248.

Jiang, Y., Sehitoglu, H., 1994. Multiaxial cyclic ratcheting under multiple step loading. Int. J. Plast. 10, 849–870.

Joseph, D.S., Chakraborty, P., Ghosh, S., 2010. Wavelet transformation based multi-time scaling method for crystal plasticity fe simulations under cyclic loading. Comput. Methods Appl. Mech. Eng. 199, 2177–2194.

Kammers, A.D., Daly, S., 2013. Digital image correlation under scanning electron microscopy: methodology and validation. Exp. Mech. 53, 1743–1761.

Kang, G., Dong, Y., Wang, H., Liu, Y., Cheng, X., 2010. Dislocation evolution in 316L stainless steel subjected to uniaxial ratchetting deformation. Mater. Sci. Eng., A 527, 5952–5961.

Kanit, T., Forest, S., Galliet, I., Mounoury, V., Jeulin, D., 2003. Determination of the size of the representative volume element for random composites: statistical and numerical approach. Int. J. Solids Struct. 40, 3647–3679.

Kanit, T., Nguyen, F., Forest, S., Jeulin, D., Reed, M., Singleton, S., 2006. Apparent and effective physical properties of heterogeneous materials: representativity of samples of two materials from food industry. Comput. Methods Appl. Mech. Eng. 195, 3960–3982.

Krishna, S., Hassan, T., Naceur, I.B., Sai, K., Cailletaud, G., 2009. Macro versus micro-scale constitutive models in simulating proportional and nonproportional cyclic and ratcheting responses of stainless steel 304. Int. J. Plast. 25, 1910–1949.

Lee, S.B., Lebensohn, R., Rollett, A., 2011. Modeling the viscoplastic micromechanical response of two-phase materials using Fast Fourier Transforms. Int. J. Plast. 27, 707–727.

Lim, C.B., Kim, K., Seong, J., 2009. Ratcheting and fatigue behavior of a copper alloy under uniaxial cyclic loading with mean stress. Int. J. Fatigue 31, 501–507.

Lu, J., Becker, A., Sun, W., Tanner, D., 2014. Simulation of cyclic plastic behavior of 304L steel using the crystal plasticity finite element method. Procedia Mater. Sci. 3, 135–140. https://doi.org/10.1016/j.mspro.2014.06.025.

Mary, C., Fouvry, S., 2007. Numerical prediction of fretting contact durability using energy wear approach: optimisation of finite-element model. Wear 263, 444–450.

Méric, L., Cailletaud, G., 1991. Single crystal modeling for structural calculations. Part 2: finite element implementation. J. Eng. Mater. Technol. 113.

Méric, L., Poubanne, P., Cailletaud, G., 1991. Single crystal modeling for structural calculations. Part 1 – model presentation. J. Eng. Mater. Technol. 113.

Nikulin, I., Yoshinaka, F., Sawaguchi, T., 2019. Superior fatigue life of Fe-15Mn-10Cr-8Ni-4Si seismic damping alloy under asymmetric cyclic loading with tensile mean strain. Mater. Sci. Eng., A 748, 371–378.

Ohno, N., Abdel-Karim, M., Kobayashi, M., Igari, T., 1998. Rattcheting characteristics of 316FR steel at high temperature, part I: strain-controlled ratchetting experiments and simulations. Int. J. Plast. 14, 355–372.

Ohno, N., Wang, J.D., 1993. Kinematic hardening rules with critical state of dynamic recovery, part II: application to experiments of ratcheting behavior. Int. J. Plast. 9, 391–403.
Osipov, N., Gourgues-Lorenzon, A.F., Marini, B., Mounoury, V., Nguyen, F., Cailletaud, G., 2008. FE modelling of bainitic steels using crystal plasticity. Philos. Mag. 88, 3757–3777.
Park, S.J., Kim, K.S., Kim, H.S., 2007. Ratcheting behaviour and mean stress considerations in uniaxial low-cycle fatigue of Inconel 718 at 649°</mathtotext>C. Fatigue Fract. Eng. Mater. Struct. 30, 1076–1083.
Pécheur, A.L., Curtit, F., Clavel, M., Stephan, J., Rey, C., Bompard, P., 2012. Polycrystal modelling of fatigue: pre-hardening and surface roughness effects on damage initiation for 304L stainless steel. Int. J. Fatigue 45, 48–60.
Pellissier-Tanon, A., Bernard, J., Amzallag, C., Rabbe, P., 1982. Evaluation of the resistance of type 316 stainless steel against progressive deformation. In: Low-Cycle Fatigue and Life Prediction. ASTM International, pp. 69–80.
Portier, L., Calloch, S., Marquis, D., Geyer, P., 2000. Ratchetting under tension–torsion loadings: experiments and modelling. Int. J. Plast. 16, 303–335.
Prithivirajan, V., Sangid, M.D., 2018. The role of defects and critical pore size analysis in the fatigue response of additively manufactured IN718 via crystal plasticity. Mater. Des. 150, 139–153.
Rovinelli, A., Sangid, M.D., Proudhon, H., Ludwig, W., 2014. Using machine learning and a data-driven approach to identify the small fatigue crack driving force in polycrystalline materials. NPJ Comput. Mater. 4.
Rycroft, C., 2009. Voro++: a Three-Dimensional Voronoi Cell Library in C++.
Sai, K., Cailletaud, G., 2007. Multi-mechanism models for the description of ratchetting: effect of the scale transition rule and of the coupling between hardening variables. Int. J. Plast. 23, 1589–1617.
Schwartz, J., Fandeur, O., Rey, C., 2013. Numerical approach of cyclic behaviour of 316LN stainless steel based on a polycrystal modelling including strain gradients. Int. J. Fatigue 55, 202–212.
Shenoy, M., Tjiptowidjojo, Y., McDowell, D., 2008. Microstructure-sensitive modeling of polycrystalline IN 100. Int. J. Plast. 24, 1694–1730 (Special Issue in Honor of Jean-Louis Chaboche).
Shenoy, M., Zhang, J., McDowell, D., 2007. Estimating fatigue sensitivity to polycrystalline Ni-base superalloy microstructures using a computational approach. Fatigue Fract. Eng. Mater. Struct. 30, 889–904.
Sinha, S., Ghosh, S., 2006. Modeling cyclic ratcheting based fatigue life of HSLA steels using crystal plasticity FEM simulations and experiments. Int. J. Fatigue 28, 1690–1704.
Siska, F., Forest, S., Gumbsch, P., 2007. Simulations of stress–strain heterogeneities in copper thin films: texture and substrate effects. Comput. Mater. Sci. 39, 137–141.
Smith, B., Shih, D., McDowell, D., 2018. Cyclic plasticity experiments and polycrystal plasticity modeling of three distinct Ti alloy microstructures. Int. J. Plast. 101, 1–23.
Stein, C.A., Cerrone, A., Ozturk, T., Lee, S., Kenesei, P., Tucker, H., Pokharel, R., Lind, J., Hefferan, C., Suter, R.M., Ingraffea, A.R., Rollett, A.D., 2014. Fatigue crack initiation, slip localization and twin boundaries in a nickel-based superalloy. Curr. Opin. Solid State Mater. Sci. 18, 244–252 (Slip Localization and Transfer in Deformation and Fatigue of Polycrystals).
Stinville, J., Echlin, M., Texier, D., Bridier, F., Bocher, P., Pollock, T., 2016. Sub-grain scale digital image correlation by electron microscopy for polycrystalline materials during elastic and plastic deformation. Exp. Mech. 56, 197–216.
Taleb, L., Keller, C., 2018. Experimental contribution for better understanding of ratcheting in 304L SS. Int. J. Mech. Sci. 146–147, 527–535.
Walley, J.L., Wheeler, R., Uchic, M.D., Mills, M.J., 2012. In-situ mechanical testing for characterizing strain localization during deformation at elevated temperatures. Exp. Mech. 52, 405–416.
Wehner, T., Fatemi, A., 1991. Effects of mean stress on fatigue behaviour of a hardened carbon steel. Int. J. Fatigue 13, 241–248.
Xie, C.L., Ghosh, S., Groeber, M., 2004. Modeling cyclic deformation of HSLA steels using crystal plasticity. J. Eng. Mater. Technol. 126, 4.
Yu, C., Kang, G., Kan, Q., Song, D., 2013. A micromechanical constitutive model based on crystal plasticity for thermo-mechanical cyclic deformation of NiTi shape memory alloys. Int. J. Plast. 44, 161–191.
Z–set package, 2013. Non-linear Material & Structure Analysis Suite. www.zset-software.com.
Zaafarani, N., Raabe, D., Singh, R., Roters, F., Zaefferer, S., 2006. Three-dimensional investigation of the texture and microstructure below a nanoindent in a Cu single crystal using 3D EBSD and crystal plasticity finite element simulations. Acta Mater. 54, 1863–1876.
Zecevic, M., Knezevic, M., 2018. Latent hardening within the elasto-plastic self-consistent polycrystal homogenization to enable the prediction of anisotropy of aa6022-t4 sheets. Int. J. Plast. 105, 141–163.
Zecevic, M., Korkolis, Y.P., Kuwabara, T., Knezevic, M., 2016. Dual-phase steel sheets under cyclic tension–compression to large strains: experiments and crystal plasticity modeling. J. Mech. Phys. Solids 96, 65–87.
Zhang, H., Diehl, M., Roters, F., Raabe, D., 2016. A virtual laboratory using high resolution crystal plasticity simulations to determine the initial yield surface for sheet metal forming operations. Int. J. Plast. 80, 111–138.
Zhang, K.S., Ju, J.W., Li, Z., Bai, Y.L., Brocks, W., 2015. Micromechanics based fatigue life prediction of a polycrystalline metal applying crystal plasticity. Mech. Mater. 85, 16–37.
Zhang, M., Zhang, J., McDowell, D., 2007. Microstructure-based crystal plasticity modeling of cyclic deformation of Ti–6Al–4V. Int. J. Plast. 23, 1328–1348.
Zhao, Z., Ramesh, M., Raabe, D., Cuitintilde=ño, A., Radovitzky, R., 2008a. Investigation of three-dimensional aspects of grain-scale plastic surface deformation of an aluminum oligocrystal. Int. J. Plast. 24, 2278–2297.
Zhao, Z., Ramesh, M., Raabe, D., Cuitiño, A., Radovitzky, R., 2008b. Investigation of three-dimensional aspects of grain-scale plastic surface deformation of an aluminum oligocrystal. Int. J. Plast. 24, 2278–2297.